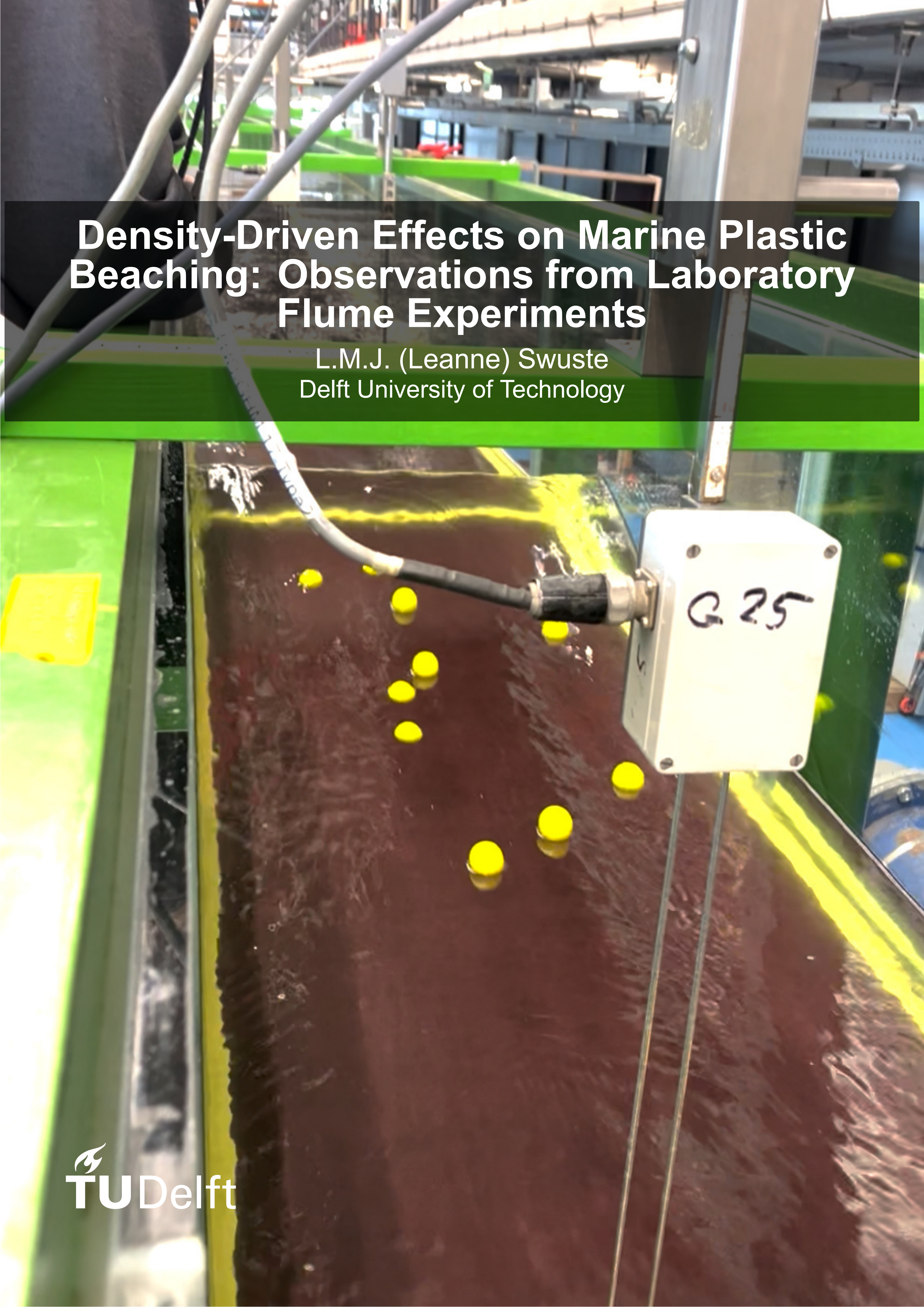

Density-Driven Effects on Marine Plastic Beaching: Observations from Laboratory Flume Experiments

L.M.J. (Leanne) Swuste
Delft University of Technology

Density-Driven Effects on Marine Plastic Beaching: Observations from Laboratory Flume Experiments

by

L.M.J. (Leanne) Swuste

to obtain the degree of Master of Science
at the Delft University of Technology,
to be defended publicly on 30th of June 2025

Student number:	5086221	
Project duration:	Februari 10, 2025 – June 30, 2025	
Thesis committee:	Dr. A (Anne) Baar	TU Delft (supervisor)
	Dr.ir. RW (Rolf) Hut	TU Delft (supervisor)
	Dr.ir. TS (Ton) van den Bremer	TU Delft (supervisor)
	Prof. dr. E. (Erik) van Sebille	UU (Advisor)
	M.E. (Marc) Schneiter	UU (Advisor)
	Dr.ir. M.A. (Matthieu) de Schipper	TU Delft (Advisor)

TUDelft

Preface

This document presents my Master's thesis on "Density-Driven Effects on Marine Plastic Beaching: Observations from Flume Experiments". This project completes my MSc in Environmental Engineering at TU Delft, within the Water Resources – Regional Hydrology track.

The objective of this thesis was to determine the effect of the density of marine plastic debris on its beaching dynamics under controlled wave conditions. An experimental campaign was conducted in the wave flume at the Waterlab at the Hydraulic Engineering Laboratory (HEL) of the Civil Engineering and Geosciences faculty of TU Delft. Throughout this experimental campaign I worked closely together with my fellow graduate student C. (Camilla) Cocozza, who focused on "The Influence of Wave Steepness on the Transport of Marine Plastic Debris in the Nearshore Environment: Insights from Laboratory Flume Experiments".

While the results shared in this report are presented as individual work, the collaboration regarding the experimental design needs to be acknowledged. The design of the experiments and the data processing methods were jointly developed. This resulted in significant shared efforts on the Theoretical Background and Methodology chapters.

This collaboration is acknowledged through this report via a colour code system. A coloured line on the left side of the text identifies which author(s) were responsible for each section.

1. Complete overlap: These sections were written in collaboration between both authors and overlaps exactly between the two MSc thesis reports.
2. Partial Overlap: These sections were originally written in collaboration by both authors but were later adapted slightly to align with the specific research questions addressed in each thesis.
3. Individual: These sections are written individually for each report by the respective author. These sections are specific for the topic addressed in this report.

A more detailed description of the collaboration efforts and the individual contribution of both students within the (partly) overlapping texts can be found below in table I.1.

L.M.J. (Leanne) Swuste
Delft, June 2025

Acknowledgement

This thesis would not have been possible without the support, guidance, and collaboration of many people, to whom I would like to extend my heartfelt thanks.

I would like to express my sincere gratitude to my supervisors, Dr. ir. R.W. (Rolf) Hut, Dr. A. (Anne) Baar, and Dr. ir. T.S. (Ton) van den Bremer, for their valuable guidance and support throughout this thesis.

Special thanks go to the Waterlab staff — C. Willems, P. van der Gaag, A. Doorn, A. van der Vlies, and Jennifer — for their technical assistance and day-to-day support in the lab. And thanks to Jimena Medina Rubio for helping out during our experimental campaign.

I am also grateful to Ir. Cem Sevindik for sharing his experimental setup and kindly adjusting his lab schedule to accommodate our work. Thanks to Dr. M.F.S. Tissier and J.A. Arriaga Garcia for providing their materials and insights related to the laboratory work used in the Ocean Waves course.

Furthermore, I would like to thank J. Mol and Dr. P. Bayle for their helpful input, particularly regarding the workings of the flume setup.

Additionally, I would like to express my gratitude to I. Haagsma, whose dedicated fieldwork at sea provided valuable results that I was able to relate to my own.

Lastly, I want to thank my flume partner, C. Cocozza, for the close collaboration, motivation, and shared commitment that made this project possible.

Abstract

Floating marine plastic debris has emerged as a major global environmental threat in recent years due to its persistence, long-distance transport, and harmful impacts on marine ecosystems. Understanding the key processes affecting plastic beaching is essential for accurately modelling plastic transport and predicting accumulation zones in nearshore marine environments. So far, research on plastic transport in shallow, nearshore waters is limited compared to deep ocean studies, resulting in significant uncertainties about wave-driven transport in these zones. While it is established that the impact of plastic density on the movement of floating plastic debris varies across wave zones, the dynamics in shallow water remain poorly understood. This research investigates how the density of finite-sized plastic particles influences the beaching dynamics under controlled, regular wave conditions in a laboratory flume simulating a nearshore environment using a sloped bathymetry. The densities relative to water of idealized spherical particles were systematically varied ranging from 0.09 to 0.93. Particles were released in the shoaling zone and tracked through the wave flume until beaching, allowing drift speeds to be analysed across different wave zones. It is observed that prior to breaking, in the shoaling zone, particles travel onshore with a speed close to the locally estimated Stokes drift regardless of the particles' relative density. In the breaking zone, density significantly affects particle drift speed: low-density particles accelerate strongly, nearing crest and phase speeds, while higher-density particles show only modest acceleration. Extending these findings to real-world coastal environments indicates that low density plastics tend to beach quickly, while denser particles remain suspended longer and thus may be affected more by lateral currents. While further research is needed to fully understand the role of density in plastic transport near the shore, this study clearly demonstrates that density significantly influences beaching dynamics—underscoring its importance in accurately modelling plastic transport in the nearshore environment.

Contents

1

Introduction

Floating marine plastic litter has rapidly become one of the most pressing environmental issues worldwide (Calvert et al. 2024). Based on population density and waste management practices, it was estimated that between 4.8 and 12.7 million tonnes of marine plastic debris (MPD) enter the oceans each year (Jambeck et al. 2015). The durability, slow degradation, and buoyancy of plastics enable their long-distance transport and accumulation over time, making them a global environmental issue. Floating marine plastic debris poses significant threats to marine ecosystems, primarily through ingestion and entanglement by marine life and through its damaging effects on sensitive habitats like coral reefs and seagrass beds. The issue can be directly linked to the Sustainable Development Goals identified by the United Nations Organisation, such as goal number 14 ”Life below Water” (Poulain-Zarcos et al. 2024). This global recognition of marine plastic pollution as a critical issue highlights the need for coordinated international action and sustainable solutions to protect the health of ocean ecosystems.

This recognition has led to growing research interest in plastic pollution over recent years. There is currently a significant discrepancy between the estimated 5–13 million tonnes of land-based plastic entering coastal waters each year (Jambeck et al. 2015) and the much smaller estimated amount of plastic observed floating at sea of less than 0.3 million tonnes (Cózar et al. 2014; Eriksen et al. 2014; Van Sebille, Wilcox, et al. 2015). To better address the plastic pollution problem, an improved understanding of physical processes that influence the transport of plastics on the surface of the oceans is required (Van Sebille, Aliani, et al. 2020). One of the areas that is still poorly understood is the dynamics along the coastlines. Laboratory studies examining the interaction between plastics and coastlines (shallow water with changing water depth) are relatively limited compared to the extensive research on plastic transport in open oceans (deep water), leading to significant uncertainties in understanding and predicting the global plastic budget (Poulain-Zarcos et al. 2024). This knowledge gap is reflected in current numerical models of plastic transport. These models often exclude detailed coastal dynamics, such as plastic beaching and resuspension, and instead rely on probabilistic methods to represent these nearshore processes (Alsina et al. 2020; Li et al. 2023). As a result, model accuracy in predicting plastic movement near coastlines remains limited.

Research conducted by Onink et al. (2021) modelled plastic transport in coastal regions and concluded that at least 77% of the positively buoyant plastic particles that are resuspended remain in near-coastal waters or beaches. This shows that coastlines and coastal waters are important reservoirs of marine plastic debris. Coastlines act as both a source and sink of plastic debris, adding complexity to the transport dynamics for plastic pollutants as beached plastics are susceptible to resuspension (Poulain-Zarcos et al. 2024). Field data research near coastlines shows variability in mean beaching times for plastics, linked to the complex influences of wind, waves, currents and other variables affecting the dynamics (Critchell et al. 2015; Kaandorp et al. 2020; Poulain-Zarcos et al. 2024). According to Poulain-Zarcos et al. (2024), in field research, the role of wave-driven processes is often assumed to be subsumed in the speed generated by wind. Therefore, the effects of wave-driven processes, such as Stokes drift and the influence of breaking waves and turbulence in the surf and swash zones, are ignored. Stokes drift refers to the net forward movement of fluid particles caused by the orbital motion of waves, resulting in a small but cumulative transport in the direction of wave propagation. Yet, in coastal regions, waves—alongside wind and ocean currents—are recognised as primary drivers of nearshore flow. Given the limited attention to the individual contribution of wave-driven mechanisms, this research aims to isolate and examine the specific role of wave-driven processes in the transport and beaching of plastic particles in the coastal region.

In the nearshore region, waves undergo key transformations as they move toward the coast. Initially, in deep-water conditions, the waves are linear. As they approach the shore, water depth decreases, which results in an increase of wave steepness and the waves becoming increasingly non-linear due to friction with the bottom, which is called shoaling. When the steepness reaches a critical threshold, the waves begin to break in the breaking zone. After breaking, the wave continues shoreward as a turbulent bore, gradually losing energy until it dissipates entirely on the beach.

Research in both deep, intermediate and shallow water have noted that transport behaviour changes throughout these different transitional zones. Studies by Calvert et al. (2024), Deike et al. (2017), Eeltink et al. (2023), Alsina et al. (2020) and Lenain et al. (2019) show that the drift speed of plastic particles can be estimated to be equal to the estimations of local Stokes drift for non-breaking waves or prior to wave breaking. Moreover, Calvert et al. (2024), Deike et al. (2017), and Lenain et al. (2019) demonstrate that the drift speed of marine plastic debris (MPD) can increase by an order of magnitude in regions affected by wave breaking, compared to the predicted Stokes drift at the same location.

Size, shape, and density are seen as key particle characteristics influencing transport behaviours. The relationship between particle density and transport, particularly in coastal zones, remains poorly understood. Particle size is important as plastics appear in the oceans as micro-, meso- and macroplastics, which impacts the effect of these plastics particles within the environment they end up in. Also, research by Xiao et al. (2025) and Calvert et al. (2024) concludes that drift enhancement can be found as particles increase in size. Research conducted by Li et al. (2023) concluded that the effect of shape on the drifting of plastic particles is found to be limited. However, more irregularly shaped FMD experience longer interactions with turbulence in the surf zone and may align with a preferred movement angle under wave action. Studies show that density effects vary across wave zones, but shallow water dynamics remain unclear. This research focuses on particle density to address this gap.

The growing body of literature highlights varying effects of plastic density on wave-driven transport. Alsina et al. (2020) observed that the density of floating particles-particles with positive buoyancy—does not appear to influence drift speeds under intermediate-depth wave conditions. However, it remains uncertain whether the observed density-independence of drift speed for positively buoyant particles under non-breaking waves persists in shallow water conditions where waves interact with a beach or slope.

Calvert et al. (2024) suggests that in the case of non-breaking waves, density may only begin to affect drift speeds as particles approach neutral buoyancy. Positively buoyant particles are positioned near the top of the water column, favouring onshore motion in wave-driven flow, resulting in particles having a greater tendency to reach the shoreline and accumulate near the furthest onshore reach of wave run-up. However, for near-neutrally buoyant particles it is suggested that density does become important due to the effects of the particles being submerged into the water column by wave action. This suggests a potential threshold or shift in the influence of density, particularly at the higher end of the relative density spectrum, about which exact relations remain unclear. Both Alsina et al. (2020) and Calvert et al. (2024) emphasise the need for further research into the role of density.

Moreover, as mentioned above, several studies report that wave breaking can increase the drift speed of marine plastic debris by up to an order of magnitude compared to Stokes drift (Calvert et al. 2024; Deike et al. 2017; Lenain et al. 2019). However, these findings are limited to particles with relatively high densities (approximately 0.9 [-]) and do not address how drift enhancement from wave breaking may vary with particle density, a factor that could significantly influence the observed acceleration. Lastly, these studies were done for deep-water breaking waves rather than shallow-water conditions over a slope, which could potentially also affect the transport dynamics.

Based on the studies discussed above, it can be concluded that the effect of density on wave-driven transport in the nearshore region remains poorly understood, which has led to the main research question of this study which can be summarised in the following question:

”What is the effect of the density of marine plastic debris on its beaching dynamics under controlled wave conditions?”

This study investigates how particle density influences the beaching dynamics of plastic debris in coastal environments. The term ”beaching dynamics” refers to understanding the sequence of particle behaviour as plastic particles move towards the shoreline under wave forcing. This includes the horizontal transport of particles along the flume (x-direction), consisting of the total transport time and the effects of interactions with waves propagating through different transformational states throughout the increasing shallow water conditions. To isolate the effect of density, laboratory experiments were conducted using controlled wave conditions over a sloped bed.

To answer the main research question, several aspects have to be considered:

- What is the relationship between particle density and total transport time under constant wave forcing?
- What is the relationship between particle density and transport dynamics across the different wave transformation zones—shoaling, breaking, and the surf zone?
- At what location along the flume do particles of different densities begin to accelerate significantly, and is there a consistent pattern across densities?
- How well do wave propagation velocities, such as Stokes drift, Phase speed and crest speed, explain the observed particle drift through different wave transitional zones for different particle density categories?
- Is there a certain density threshold beyond which the beaching behaviour of particles changes abruptly, suggesting a shift in transport dynamics?

Li et al. (2023) conducted research closely related to this research. This study states that the density of MPD can range from 0.05 g/cm^3 to 2.3 g/cm^3 due to the large variety of polymer types and manufacturing processes. Their research consisted of a laboratory study in a wave flume generator using one wave condition and rigid cubes states that for varying densities. It was concluded that for higher-density particles it takes longer to reach the beach and the particles migrate less far up onto the beach. When the density of the particle is less than half the density of the water, the particle becomes less likely to beach at all and remains in the coastal region. However, this research focuses solely on a single wave type (characterised by a specific wave height, steepness, and water depth) and is limited to the study of rigid cubes. Additionally, a temporal limit was applied, which led to certain density categories never reaching the beach. In contrast, the current research adopts a spatial limit to capture the full range of particle transport and beaching behaviour. Therefore, this research, focusing on the impact of varying densities, could strengthen and expand upon the findings of the study conducted by Li et al. (2023). Based on this and previous research, higher particle density is expected to reduce drift speed and make beaching more difficult, where the strongest effect is expected to appear in the breaking zone.

Understanding plastic deposition and resuspension is crucial for identifying accumulation zones and improving knowledge of plastic movement in marine environments. Key processes—such as when and where plastic beaches, why some beach while others drift offshore, and what conditions trigger resuspension—are still poorly understood. These dynamics are essential for developing accurate models of plastic transport. For such models to be effective, they must be well-parametrised based on a detailed understanding of the underlying physical processes. These insights are vital for informing mitigation strategies, including targeted plastic removal efforts in coastal areas (Van Sebille, Aliani, et al. 2020).

This report begins by outlining the key concepts necessary to understand the context and implications of the research in Chapter 2. Chapter 3 describes the methodology used throughout the study. The results, including estimated drift speeds along the flume, are presented in Chapter 4. Chapter 5 discusses the main findings, addresses key assumptions and sources of uncertainty, and concludes with recommendations for future research. Chapter 6 summarises the main findings of the research and answers the questions mentioned above.

2

Theoretical Background

This chapter provides the background needed to follow the analysis in this research. It introduces the type of marine plastic debris studied and outlines key wave concepts, including basic wave parameters, coastal dynamics, and wave propagation velocities, which include phase speed, crest speed and Stokes drift.

2.1. Marine Plastic Debris

Marine plastic debris (MPD) is defined as waste created by human activities entering the marine ecosystem. It consists of mixtures of particles with varying size, shape and chemical composition (Van Sebille, Aliani, et al. 2020) which can be found floating on the surface, suspended in the water column, or deposited on the seabed. The primary contributors to MPD are land-based sources such as mismanaged waste and urban run-off, which reach the marine environments through river discharge. Sea-based sources, on the other hand, consist of fishing, shipping and touristic activities, which cause direct delivery of plastic particles into the sea (Löhr et al. 2017).

The characteristics of MPD is subject to change over time due to multiple processes, such as embrittlement, fragmentation, bio-fouling, weathering and erosion (Van Sebille, Aliani, et al. 2020). The physical, chemical, and biological processes in the ocean can alter the size, shape, and density of plastic debris. These changes, along with the MPD original characteristics, lead to a wide range of variations in their size, shape, and density.

This research specifically focuses on floating macroplastic particles larger than 5 millimetres, with densities lower than that of seawater, giving them positive buoyancy, meaning they experience an upward force that causes them to float. It is important to note that 'floating plastic' does not consistently remain at the surface; it may temporarily submerge due to ocean turbulence and breaking waves. Nevertheless, owing to its positive buoyancy, it will ascend back to the surface.

2.2. Wave Basics

This research focuses on the behaviour of ocean waves as they approach the shoreline, particularly in the context of the interaction of waves with plastic particles. To understand these dynamics, it is essential to first introduce the fundamental characteristics of ocean waves and the theoretical framework used to describe them.

Waves can be described as disturbances that move through a material, such as water, over time and space. These disturbances typically occur over distances and times much larger than the wave's own wavelength and period (Holthuijsen 2007). In this context, a wave refers to the vertical movement of the water surface. In natural ocean settings, ocean wave behaviour is influenced by multiple interacting forces, including wind, tides, and currents. These factors can significantly affect wave transformation and particle transport. These dynamics and transformations make the study of waves complex, especially in coastal areas, and thus waves are typically assumed to be sinusoidal, periodic waves under idealised conditions, which allows for simplified mathematical descriptions such as linear wave theory.

The main key parameters used throughout this study include:

- **Wave height** (H): the vertical distance from trough to crest.
- **Wave period** (T): the time it takes for two successive wave crests to pass a fixed point.
- **Water depth** (h): the vertical distance from the still water surface to the seabed.
- **Wavelength** (λ): the distance between two consecutive wave crests or troughs. The wavelength depends on the water depth and the wave period.
- **Wave frequency** (f): the inverse of the period, $f = \frac{1}{T}$.
- **Wave number** (k): defined as $k = \frac{2\pi}{\lambda}$.
- **Angular frequency** (ω): given by $\omega = 2\pi f$.

This research involved the generation of a train of regular, or monochromatic, waves. The term monochromatic wave refers to the simplest type of wave, characterised by a single value of wave height and wave period. This kind of wave is typically employed in laboratory flume studies. If the wave's height is small enough compared to its wavelength, its behaviour can be approximated to a sinusoidal variation in surface water elevation and therefore described by linear wave theory (Soulsby 1997).

Given the use of a regular wave train, the wave conditions in this research are fully defined by specifying three input parameters: the wave period (T), water depth (h), and wave height (H). Once these primary parameters are known, all other key wave characteristics—such as wavelength and dimensionless numbers like the Ursell and Iribarren numbers—can be derived using established theoretical relationships. The following section presents the relevant formulas used to compute the mentioned parameters.

2.2.1. Wavelength

The wavelength L refers to the horizontal distance between two successive wave crests. The dispersion relationship in Equation 2.1 provides an approximation of the wavelength based on wave period and water depth, as wave motion is influenced by both gravity and depth-dependent restoring forces.

$$L = \frac{gT^2}{2\pi} \tanh\left(\frac{2\pi d}{L}\right) \tag{2.1}$$

Where:

- L = wavelength [m]
- g = gravitational acceleration (≈ 9.81 m/s^2)
- T = wave period [s]
- d = water depth [m]

This is an implicit expression which requires an iterative procedure to approximate the wavelength for a given period and depth. Explicit expressions that approximate the solution are available and widely used; in this context the Fenton approximation (1988) was applied (Fenton 1988). Formula 2.2 describes the Fenton approximation (Holthuijsen 2007).

$$kd \approx \frac{\alpha + \beta^2 (\cosh \beta)^{-2}}{\tanh \beta + \beta (\cosh \beta)^{-2}} \tag{2.2}$$

This approximation takes the linear dispersion relation and corrects it for a depth-dependent term. It works well for the varying water depths used in the setup. The solution computed with this method is exact for deep-water and shallow-water regimes and presents an error in wave number (k) which is less than 0.05% in all other conditions. The method consists in solving equation 2.1. To use formula 2.2, the parameters α and β need to be determined. To do so, L_0 and k_0 are to be computed as deep-water approximations of the wavelength and wave number by using relations 2.3 and 2.4.

$$L_0 = \frac{gT^2}{2\pi} \tag{2.3}$$

$$k_0 = \frac{2\pi}{L_0} \tag{2.4}$$

Factor α can be obtained from the previously computed k_0 by solving equation 2.5.

$$\alpha = k_0 h = \frac{4\pi^2 d}{gT^2} \tag{2.5}$$

Factor β can be then obtained from α by solving equation 2.6.

$$\beta = \alpha (\tanh \alpha)^{-1/2} \tag{2.6}$$

From the result of the Fenton relation, 2.2, the approximation for the wavelength can be eventually obtained using equation 2.7.

$$L = \frac{2\pi h}{kd} \tag{2.7}$$

2.2.2. Wave Steepness

Wave steepness describes the ratio between the wave height (H) and the wavelength (L), representing how ”steep” the wave profile is. Offshore steepness refers to this ratio in deep water before the wave begins to transform due to its interaction with the sloped bottom throughout regions with decreasing depth. The offshore steepness can be estimated using the definition presented in 2.8.

$$steepness = a \cdot k = \frac{H}{2} \cdot \frac{2\pi}{L} = \frac{\pi H}{L} \tag{2.8}$$

2.2.3. Ursell Number

The Ursell number is defined as a dimensionless parameter that helps determine wave breaking. For the wave conditions used in this study, the Ursell number was assessed to ensure that the waves do not break immediately at the wave paddle. In the context of the current study, an Ursell number value below a threshold of 25 ensures that the waves remain in non-breaking conditions as they leave the wave generator paddle (Holthuijsen 2007).

The Ursell number was determined using the formula 2.9.

$$U_r = \frac{H_0 \cdot L^2}{h^3} \leq 25 \tag{2.9}$$

where H_0 is the wave height in metres, h is the water depth in metres and L is the wavelength in metres which has to be large compared to the depth (L»h).

2.2.4. Validity Domain

To ensure proper wave generation in the flume to comply with the operational constraints of the wave maker, the input wave conditions were checked to fall within the valid range of linear or second-order Stokes wave theory. This was done by calculating the relative depth and wave steepness (Equations 2.10 and 2.11) and comparing them to known theory limits. Figure 2.1 shows that the tested conditions fall within an acceptable range for the experiment.

$$relative\_depth = \frac{h}{gT^2} \tag{2.10}$$

$$relative\_steepness = \frac{H}{gT^2} \tag{2.11}$$

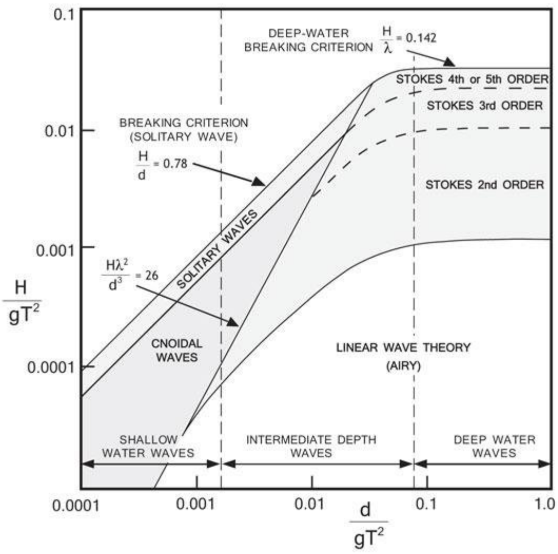

Figure 2.1: Ranges of applicability of the various wave theories (Holthuijsen 2007).

2.2.5. Iribarren number

Wave breaking is the most non-linear process influencing waves in coastal waters (Holthuijsen 2007). To predict the type of breaking, empirical formulas are often used—most notably, the Iribarren number, which serves as a key indicator for distinguishing between different breaker types. This dimensionless parameter is used to distinguish between spilling, plunging, collapsing, or surging waves. Spilling breakers occur on gentle slopes and gradually lose energy as the wave crest spills forward. Plunging breakers are more energetic and form a curling motion with a sudden crash, typically seen on moderate slopes. Collapsing and surging breakers appear on steep slopes and do not break in the traditional sense but rush up the slope at high speed. Identifying the breaker type was relevant as it indicates the energy dissipation and coastal or experimental wave dynamics. The Iribarren number was calculated using Formula 2.12.

$$\xi_0 = \frac{\tan\alpha}{\sqrt{H_0/L_0}} \tag{2.12}$$

Where ξ_0 is the Iribarren number, α is the beach slope angle, H_0 is the deep-water wave height and L_0 is the deep-water wavelength.

in which:

$$\begin{aligned} \textit{spilling:} &\quad \text{if } \xi_\infty < 0.5 \\ \textit{plunging:} &\quad \text{if } 0.5 < \xi_\infty < 3.3 \\ \textit{collapsing or surging:} &\quad \text{if } \xi_\infty > 3.3 \end{aligned}$$

2.3. Coastal Wave Dynamics

During the propagation from deep water to the shoreline, waves undergo major changes in shape due to the interaction with the seabed (Alsina et al. 2020).

Deep-water waves approaching the shore start to feel the presence of the seabed, where friction and decreasing depth trigger a non-linear evolution of the waves. As waves approach shallower water, their height increases and their shape becomes horizontally asymmetric, with steep crests and flatter troughs—a process known as shoaling. As waves move further towards the shore, the steepness of the wave front continues to increase, causing instability and eventually degenerating into wave breaking. The breaking front of the wave (surf bore) starts dissipating wave energy while propagating shoreward. Once the shore is reached, friction and gravitational forces cause the surf bore to decelerate and run up on the beach. As the forward motion ceases, water accelerates in the offshore direction during the backwash phase concluding the beach run-up/run-down process. All the mentioned interactions between wave energy and shoreline take place in the nearshore environment (Van der Zanden 2016; Van Sebille, Aliani, et al. 2020) and are visualised in Figure 2.2.

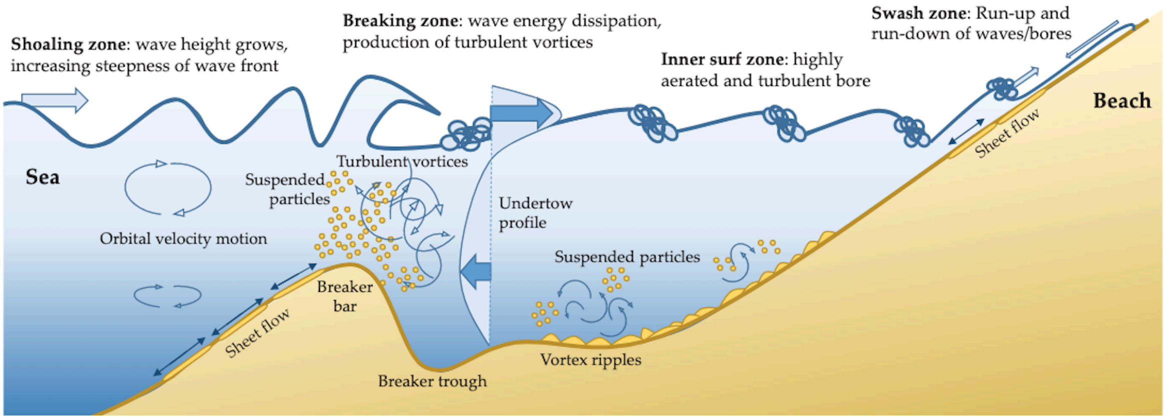

Figure 2.2: Conceptual representation of cross-shore processes in the near-shore region from (Van der Zanden 2016).

2.4. Wave Propagation Velocities

To better understand the driving mechanisms behind particle transport, the drift velocities of the MPD were compared to characteristic wave propagation speeds. This comparison helps to place the observed particle dynamics in the broader context of wave-particle interactions. The term wave propagation speed refers to the different characteristic speeds at which different components of a wave field move. Within this research this includes the phase speed, crest speed and Stokes drift. The definition of these components is given in the following sections.

2.4.1. Phase and Crest Speed

The phase speed refers to the speed at which a specific phase of the wave travels. Crest speed is the actual speed of the crest itself. For waves that can be described using linear wave theory, the phase speed can be determined using Formula 2.13.

$$c = \frac{\omega}{k} = \sqrt{\frac{g}{k}\tanh(kh)} \tag{2.13}$$

In which:

- c is the phase speed [m/s],
- ω is the angular frequency [rad/s],
- k is the wave number [rad/m].
- h is the water depth [m].
- and g is the gravitational constant $[m/s^2]$

This formula can be rewritten to be expressed in terms of wave height, water depth and wave period, which results in 2.14.

$$c = \left(\frac{gT}{2\pi}\right)\tanh\left(\frac{2\pi h}{L}\right) \tag{2.14}$$

For linear waves in deep water, the crest speed is expected to match the phase speed as the wave maintains its shape as it propagates. Waves become increasingly non-linear as they propagate shoreward, the phase speed for non-linear waves is then expected to be higher (Tissier et al. 2011). Linear wave theory allows for a reasonable description of wave celerity for deep water, nonetheless, corrections are needed to account for non-linearities during the shoreward movement.

Formulation 2.15 asymptotically approaches the non-linear dispersion relation derived by Hedges (1976) for shallow water, with the modification introduced by Booij (1981) (Martins et al. 2021). This appears to be an upper bound for the propagation speed of wave components in the surf zone (Martins et al. 2021).

$$c = \sqrt{gh\,(1+\varepsilon)} \tag{2.15}$$

In which:

- c is the non-linear phase speed [m/s],
- g is the gravitational constant $[m/s^2]$,
- h is the water depth [m],
- ε is the local wave steepness [-].

2.4.2. Stokes Drift

The Stokes drift refers to the net drift speed in the wave propagation direction, experienced by a particle floating on the free surface of a surface gravity wave (Van Sebille, Aliani, et al. 2020). In other words, the Stokes drift speed is the difference between the average Lagrangian flow velocity (velocity at which the particle moves) and the average Eulerian flow velocity of the fluid (velocity at which the water moves) (Van Sebille, Aliani, et al. 2020). This happens as particles exposed to a surface wave field travel faster at the top of their orbits than at the bottom, and thus spend more time in crests where their velocity is positive (Van Sebille, Aliani, et al. 2020). Stokes drift depends on the shape of the wave; it is proportional to the square of the wave steepness, defined as wave height over wavelength (Soulsby 1997). In coastal areas where waves increase in steepness until they break, the Stokes drift can be especially important for MPD transport.

The Stokes drift can be estimated by applying the derivation for general water depth formalised by Ursell and presented in Equation 2.16 (Van den Bremer et al. 2017). This expression is referred to as ”mass-transport velocity” and describes the net motion in the direction of wave propagation.

$$\overline{U} = \frac{a^2 \sigma k \cosh 2k(z-h)}{2 \sinh^2 kh} \tag{2.16}$$

Where:

- $\overline{U}$ is the Stokes drift velocity at elevation z
- a is the wave amplitude
- σ is the angular frequency of the wave
- k is the wave number
- z is the vertical coordinate (z = 0)
- h is the water depth

Legend: ▬ 100% overlap ▬ 90% overlap with minimal adjustments ▬ 0% overlap

3

Methodology

This chapter presents the methodology used to investigate the influence of particle density on the beaching behaviour of plastic debris in a laboratory flume. A controlled laboratory setup was chosen to isolate particle density as a variable and minimise the influence of external environmental factors. The experimental setup is described in detail to provide a reproducible account of how this research was conducted. The physical setup of the flume is presented, as well as the tested wave conditions, the particles used and the different measurement tools. In addition, the use of the SWASH numerical model to simulate wave conditions and guide the design of the experimental campaign is justified and explained in this context.

3.1. Experimental Setup

The defined research question ”*What is the effect of the density of marine plastic debris on its beaching dynamics under controlled wave conditions*” was addressed by conducting experiments in a controlled laboratory flume at the Hydraulic Engineering Laboratory (HEL) of the Civil Engineering and Geosciences faculty of TU Delft.

During the data collection phase, plastic particles were placed into the flume before the wave’s breaking point, and their trajectory was tracked until they stabilised on the slope and were considered beached. Multiple experimental runs were conducted using different sets of plastic particles, each with a specific density, to assess how particle density affects beaching behaviour. In the following sections, the experimental setup, measurement tools, and procedure are described in further detail.

3.1.1. Experimental Facility

The experiments were carried out in the Wave Flume (WF) presented on the left-hand side of Figure 3.1, available at the HEL as a state-of-the-art wave flume for (MSc) education and research (TU Delft Faculty of Civil Engineering and Geosciences n.d.). The flume presents effective dimensions of 39 metre in length, 0.79 metres in width and 1 metre in height.

Waves can be generated inside the flume using an electrically controlled piston-type wave generator with a maximum stroke of 2 metres allowing the piston to move up to 2 metres horizontally during its oscillation cycle. The wave generator is capable of reproducing a wide range of wave types and conditions, defined by the user through a user-friendly interface. The machine is equipped with an Active Reflection Compensation system (ARC) which can be activated to minimise wave reflection by dynamically adjusting the motion of the piston.

Preliminary experiments were conducted in the Sediment Flume of the HEL, shown on the right-hand side of Figure 3.1. This flume presents similar dimensions as the Wave Flume (length: 39.0 metres, width: 0.76 metres, height: 0.85 metres) and is equipped with an equivalent wave generation system.

The similarities between the two flumes allowed for the testing and familiarisation of the available equipment as well as the definition of the experimental design for the data collection campaign before its actual start.

Figure 3.1: Wave Flume (left) and Sediment Flume (right) inside the Hydraulic Engineering Laboratory of TU Delft (TU Delft Faculty of Civil Engineering and Geosciences n.d.)

3.1.2. Wave Flume Bathymetry

The Wave Flume, in its original condition, presented a flat bottom. For this experimental campaign, a timber slope was installed inside the flume to simulate a beach profile. The bed was kept horizontal for the first 8 metres. This first flat section was followed by a 1:40 slope, gradually rising to a final height of 60 cm, as illustrated in Figure 3.2. The timber slope has a smooth veneered surface, smoother than most real beaches, as they consist of sand or gravel. This difference in roughness can affect the dynamics of how the waves and the plastics interact with the surface compared to the real world. However, a timber slope was chosen due to practical and technical constraints associated with replicating a sand beach in the flume environment.

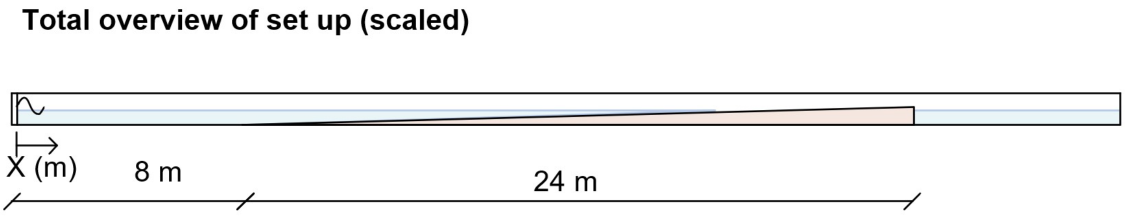

Figure 3.2: Schematic showing the beach profile dimensions within the flume scaled to reality

3.1.3. Wave Gauges

Six wave gauges for the measurement of dynamically varying water levels were installed along the horizontal direction of the flume as depicted in Figure 3.3. The instruments consist of a probe and a control unit. In these electric conductivity-based wave gauges, the probe is made of two parallel stainless steel rods which function as electrodes. The sensor outputs an analogue signal expressed in volts that is linearly related to the water level between the rods. The control unit supplies the metre with power and presents a dial which allows for adjustments in the wave height metre to perform the desired calibration.

A calibration phase was conducted to calculate the factors required to linearly link the recorded voltage to surface elevation values in metres. The factors were computed by gradually varying the water level inside the flume in regular steps, recording the measured voltage and dividing the applied increase in water level by the measured voltage. The average of the factors for each step was calculated and used as the final factor for the conversion between measured voltage and surface elevation. Equation 3.1 was applied for the conversion, where η refers to the surface elevation in metres and x to the measured value in volts. The factors resulting from the calibration are presented in Table 3.1.

$$\eta = factor * x \tag{3.1}$$

Table 3.1: Conversion factors for six wave gauges

Wave Gauge	Conversion Factor [m/V]
1	0.0253
2	0.0248
3	0.0249
4	0.0245
5	0.0244
6	0.00502

A single wave condition was used, and the six wave gauge locations were chosen to ensure broad spatial coverage and to effectively capture the wave transformation along the slope. A representation of the flume with the measuring locations, including the breaking point of the used wave condition is presented in Figure 3.3. The exact positioning of the instruments is also presented in 3.2. The deployment strategy of the wave gauges is described in Section C.2.

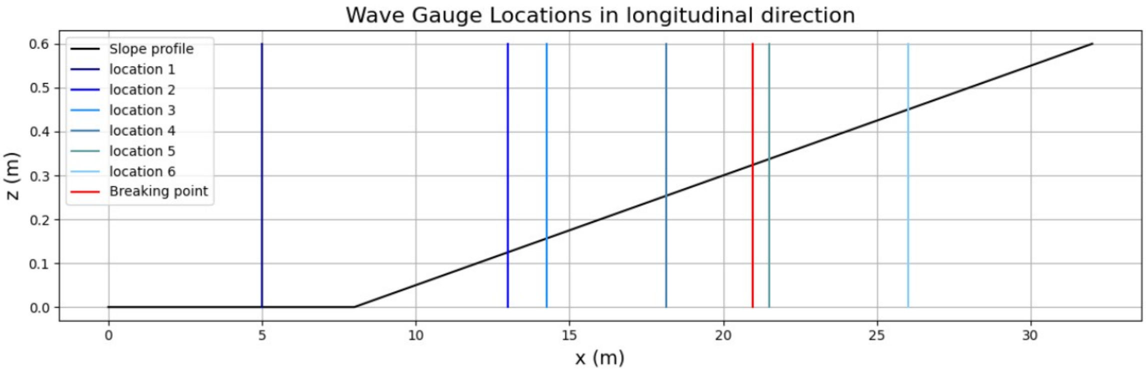

Figure 3.3: Representation of flume setup with measuring locations.

Location	x location [m]	Depth above bottom [m]
Location 1	5	0.235
Location 2	13	0.18
Location 3	14.25	0.15
Location 4	18.15	0.06
Location 5	21.5	0.06
Location 6	26	0.003

Table 3.2: Placement depths of wave gauges (WG) at different x_f locations along the flume.

3.1.4. Camera setup

To analyse particle movement throughout the flume, six GoPro cameras were used — three mounted overhead to capture the top view, and three positioned along the side to record the side profile. Two GoPros model Hero7 and four GoPros model Hero 10 were used, which were all set to record at 30 frames per second in Linear mode in 4k resolution. To allow the cameras to operate for an extended period of time, their batteries were removed and they were connected to power outlets using USB-C cables. The GoPros were connected to the GoPro Quik app, allowing remote operation using a phone. The video recordings were saved on SD cards and were transferred to hard drives at the end of each set of runs. The GoPro models Hero7 and Hero10 vary slightly in terms of camera consistency (field of view, colour profiles, distortion), which might result in slight differences in video footage. To ensure colour consistency for the colour-based tracking algorithm, three identical GoPro Hero10 cameras were used for the top view, as these were used for quantitative analysis of the particles' trajectories and therefore required particular attention.

Concerning the top-view cameras, three GoPros were used to capture footage from above. The overhead cameras were attached under a 12-metre wooden beam spanning over the shoaling zone to the beaching location. The cameras were secured to the underside of the beam, which had been tested to ensure it was level. The beam was positioned at a height of 2.15 metres above the bottom of the flume, centred along the width of the flume. This setup allowed the cameras to capture a 3-metre long section of the flume in the x-direction while ensuring optimal particle visibility for tracking purposes. A schematic of the setup is shown in Figure 3.4

The exact placement of the cameras along the flume (x-direction) was determined based on the beaching location and the breaking point of the wave condition. To ensure continuous particle tracking, the camera view windows were strategically positioned to have overlap between the different videos. With three top-view cameras, this setup provided complete coverage of a stretch of approximately 9 metres of the flume.

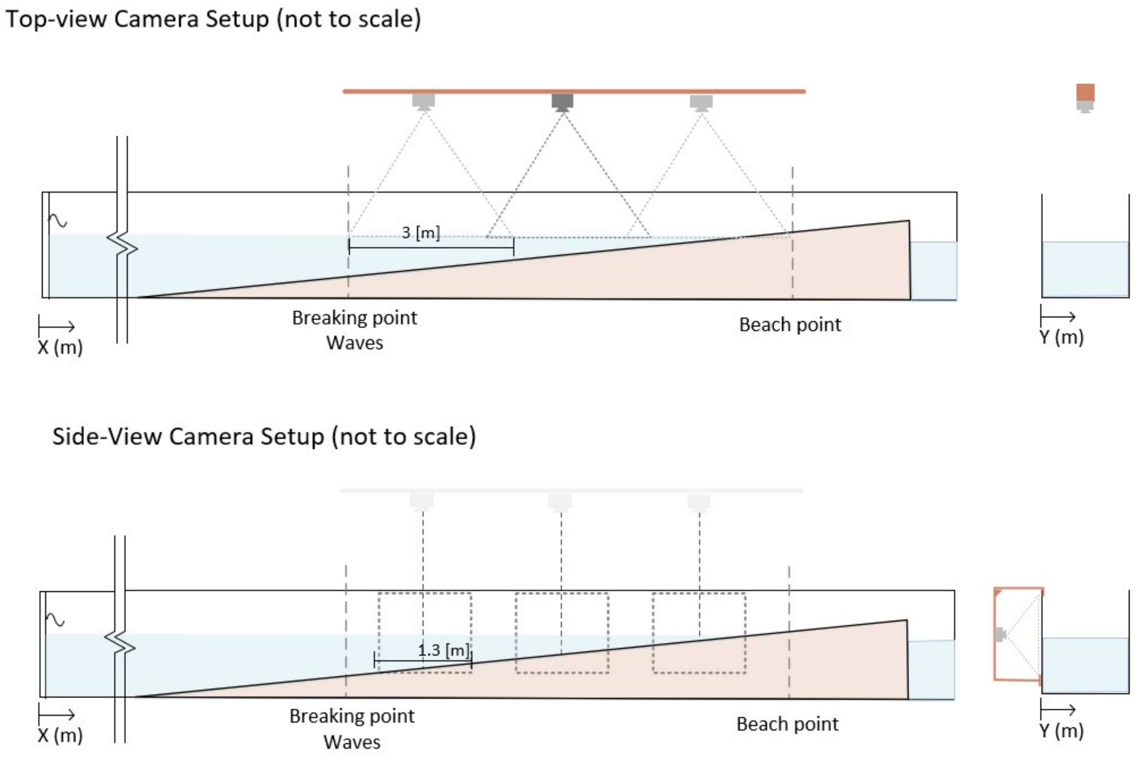

Figure 3.4: Schematic showing placement of the cameras in longitudinal direction and as a cross section along the length of the flume

The side-view cameras were aligned with the same cross-sections as the top-view cameras to maintain spatial consistency between both perspectives, as illustrated in Figure 3.4. These cameras were mounted on a wooden frame placed 0.9 metres away from the glass wall of the flume. Due to this relatively short distance, each camera's field of view covered approximately 1.3 metres in width. As a result, the side-view cameras captured only a portion of the total travel distance of the particles within the flume. However, the missing segments were not considered problematic as the recordings from the side-view cameras were not used for particle tracking. Instead, these videos served as a tool for qualitative analysis. Specifically, the side-view recordings were used for observational purposes to visually inspect the flow and particle behaviour, especially in cases where the top-view recordings indicated unusual or unexpected behaviour.

A camera calibration process was performed to avoid any image distortion; the specifics of this are described in Appendix A. No relevant distortion was observed, therefore the original videos were used in the analysis. Additionally, pixel distances were related to metric distances by using reference frames indicating real-world distances visible on camera. Further elaboration on the reference frames system can be found in Appendix A.

3.2. Experimental Conditions

To isolate density as the only variable, a consistent wave condition is used, ensuring uniform wave energy across all tests and making density the sole driver of drift speed differences.

3.2.1. Wave Condition and Water level

A train of regular waves was generated in the flume. Regular waves provide a controlled and repeatable environment, making them ideal for isolating the effects of a single variable. By maintaining consistent wave characteristics, regular waves minimise variability and allow for precise comparisons between different plastic particle density categories.

The primary parameters for the wave simulations that need to be defined include:

- h: the still mean water level in the basin [m],
- T: the period of the simulated waves [s],
- H: the wave height at the wave generator [m].

Within this thesis, the still mean water level (h) was set to 0.5 metres. This decision was made based on the design of the slope. A higher water level allows for more precise wave generation by the wave maker, but the waves should not wash over the end of the slope. A water level of 0.5 metres was chosen as it balanced both of these considerations effectively.

A period of 1.5 seconds was selected, which results in a wavelength of 2.8 metres using the Fenton approximation (1988) (Holthuijsen 2007) as described in section 2.2.1.

With the given still water depth and period, the Ursell number was assessed to ensure that the chosen wave height would not result in waves that break immediately at the wave paddle. The Ursell number, described in more detail in section 2.2.3, is defined as a dimensionless parameter that helps determine wave breaking. In the context of the current study, an Ursell number value below a threshold of 25 ensures that the waves remain in non-breaking conditions as they leave the wave generator paddle. With the given still mean water level of 0.5 metres and a period of 1.5 seconds, a maximum wave height (Ursell = 25) was determined to be 0.39 metres using the formula 2.9. Waves generated in the flume with heights above 0.25 metres were observed to break prematurely, likely due to the wave maker's limitation to producing only first- and second-order Stokes waves. Therefore, a wave height of 0.11 metres was selected for this study. This value falls well within the stable, non-breaking range (0–0.25 metres) and was chosen based on both literature references and experimental observations.

Given a wave height of 0.11 metres, an offshore wave steepness-the ratio of wave height to wavelength offshore-of 0.12 can be determined using the formula given in section 2.2.2. Given this estimate, the waves can be considered relatively steep. Typical steepness values for deep-water ocean waves range from 0.02 to 0.10, with values above 0.10 occurring mainly under extreme or stormy conditions (Antrim 1981). There is a maximum limit to how steep a deep-water wave can be before it breaks, which occurs when the water particle velocity at the wave crest becomes equal to the wave's forward speed. For periodic waves, this physical limit leads to a maximum wave steepness of about 0.14 in deep water (Holthuijsen 2007). However, since the flume setup involves intermediate-to-shallow-water depths rather than deep water, these steepness values should not be directly compared; wave behaviour and breaking criteria differ significantly under such conditions.

The breaker type was determined based on the Iribarren number, which is described in more detail in section 2.2.5. This dimensionless parameter is used to distinguish between spilling, plunging, collapsing, or surging waves. Identifying the breaker type is relevant as it indicates the energy dissipation and coastal or experimental wave dynamics. The combination of the mean still water level of 0.5 metres, period of 1.5 seconds and wave height of 0.11 metres resulted in an Iribarren number of 0.13 [-]. An Iribarren number ξ of 0.13 suggests that the waves are spilling. This value indicates that the wave steepness is moderate compared to the beach slope, leading to a gradual, spilling type of wave break rather than a more abrupt plunging or collapsing break.

The combination of water depth, wave period and height results in Stokes 2nd order waves, as shown in Figure 3.5 about which further elaboration can be found in section 2.2.4.

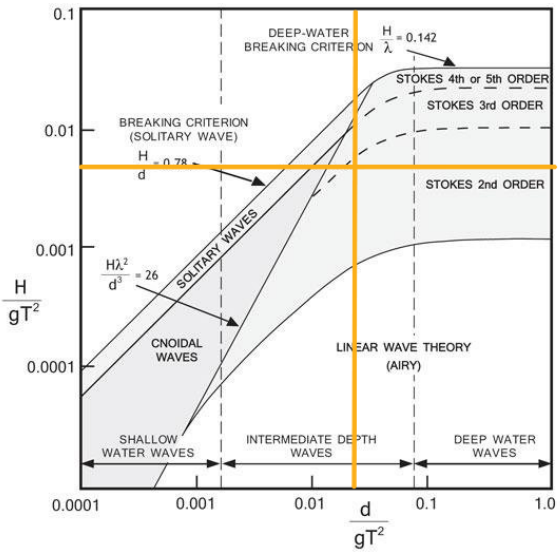

Figure 3.5: Ranges of the validity for various wave-theories (Holthuijsen 2007) showing chosen wave condition.

3.2.2. Identification of Hydrodynamic Zones in the Flume

Waves approaching the coastline experience transformations due to decreasing water depth, which can be divided into distinct zones as outlined in Section 2.3. For the given wave condition, as well as the fixed slope and flume setup used throughout the experimental campaign, the location of the breaking point and the boundaries of the different wave zones remain consistent for this setup.

Throughout this research, particles were released in the shoaling zone, near the wave breaking location. Setting $x_f = 0$ metres as the beginning of the flume, the particle release location in the shoaling zone was at $x_f = 19.5$ metres. The transition between the shoaling zone and the surf zone occurs at wave breaking. Throughout this research, this transition zone is referred to as the breaking zone; however, its exact boundaries are difficult to define.

The boundaries used in this research were based on observation in the flume. It was observed that sunken particles accumulate near where the waves break; this location is designated as the breaking point, measured at $x_f = 21$ metres. By closely observing the waves, it was determined that actual wave breaking-the point where the top of the crest starts to tip over-occurs approximately 50 cm before this accumulation point, at $x_f = 20.5$ metres. The accumulation point corresponds to where the wave height begins to decrease sharply, where it collapses onto itself over approximately another 50 cm. And thus within this research, the end of the breaking zone was set to be at $x_f = 21.5$ metres. This breaking zone is expected to be a highly energetic region in which it is expected that the floating particles will be propelled forward with the bore and will experience an acceleration.

Before the breaking zone lies the shoaling zone, where waves become increasingly non-linear. Particle transport is expected to be lower in this region, as wave energy is focused on wave steepening rather than forward momentum.

Following the breaking zone is the surf zone, where wave height gradually decreases along the flume until the water becomes shallow near the slope's end. This transition marks the start of the swash zone, estimated around $x_f = 26$ metres. As wave energy diminishes, particle transport is expected to steadily decline throughout these regions.

3.2.3. Particle design

To investigate density-dependent particle behaviour with regard to the beaching process, spherical particles were designed. All particles were spheres with a diameter of 4 centimetres with a smooth outside surface. Each category of particles had a different weight, which results in a different density given the constant size and shape. Table 3.3 shows the particle categories used within this research. This table shows the relative density values used based on the density of the particle and the density of fresh water (999.9 [kg/m^3]) since the water used in the flume is fresh water. The particles were designed to simulate buoyancy conditions encountered in saline marine environments (typically 1025 kg/m^3 for seawater) while fresh water was used (density = 999.9 kg/m^3) in the wave flume. A more detailed description of the particle fabrication is given in Appendix B.

Particle number	Color	Diameter [mm]	Weight [g]	Density [kg/m^3]	Relative Density [-]
1	yellow	40	2.95	88.0	0.09
2	yellow	40	3.08	91.9	0.09
				Average per category	0.09
3	pink	40	5.09	151.9	0.15
4	pink	40	5.06	151.0	0.15
				Average per category	0.15
5	green	40	7.66	228.6	0.23
6	green	40	7.78	232.8	0.23
				Average per category	0.23
7	pink	40	14.2	423.8	0.42
8	pink	40	13.3	398.0	0.40
				Average per category	0.41
9	green	40	23.27	694.9	0.69
10	green	40	22.95	684.9	0.68
				Average per category	0.69
11	pink	40	25.21	752.3	0.75
12	pink	40	25.19	752.1	0.75
				Average per category	0.75
13	yellow	40	31.3	934.1	0.93
				Average per category	0.93

Table 3.3: Particle characteristics among which weight [g], density [kg/m^3], and relative density [-] (particle density/ freshwater density)

All selected relative densities were below 1, as this study focuses exclusively on floating plastics. According to Newton's second law ($F = ma$), particles with higher density-and therefore greater mass-are more resistant to acceleration, which is expected to reduce their drift speed under constant wave energy. Relative densities ranged from 0.09 to 0.93 to reflect the diversity of real plastic types and to explore the relationship between density and drift speed across the full spectrum of floating materials. This stepwise approach enables a broad understanding of the density–drift speed relationship and helps identify potential thresholds where the behaviour may shift. Once this overall trend is established, future research can focus more closely on specific ranges for more detailed analysis.

3.3. Experimental Procedure

The experimental procedure was designed to observe and measure the beaching behaviour of MPD under a single wave condition.

A series of steps were systematically carried out during a preparatory phase before the start of the actual experiments. The flume was filled up until a stable water level of 0.5 metres. This water level was visually inspected using a measuring lint on the side of the flume and detected consistently by the wave generator. The measuring instruments in Location 1 were turned on from a designated computer, starting the recording of the surface elevation and velocity values which were continuously logged for the whole duration of the experimental runs.

Once the target water level was reached and the measuring instruments on, the wave generator was activated. This was programmed to replicate the desired wave condition for a total time of 45 minutes. This time frame was selected to keep the generated waves as stable as possible, avoiding them from diverging from the programmed condition in the long term. In addition, the ARC system was turned on and left on for the whole duration of the experimental runs to absorb waves reflected by the structure avoiding potential disturbances in the observed wave conditions.

The generator was left on for an initial spin-up time of five minutes before starting the measurements, the reasoning behind which is explained in further detail in section C.1. During this time no experiment was conducted to limit the influence of any initial disturbances on early measurements.

The last step of the preliminary phase consisted in remotely turning on all the installed GoPros. The six GoPros were activated at slightly different times as they had to be turned on one by one. To synchronise the recordings and establish a common reference point (t = 0 seconds) across all cameras, a sharp sound was generated at the start of the experiment. This sound, which could be heard across all six recordings, was used to temporally align the datasets.

The actual experimental procedure consisted of carefully placing the plastic particles at their designated release point inside the flume. The release point was set 1.5 metres upstream of the wave breaking location, with the reasoning detailed in section C.3. The particles were always placed from above, in the middle of the flume in the y-direction and approximately one metre before the breaking point. The travel time of the particles from the moment they entered the flume until they reached a stable position on the beach was manually measured by recording the time of placement and the time of beaching. Once beached, the particles were retrieved from the flume and placed again with a cadence that allowed for the maximisation of the number of particles travelling in one experimental run.

Due to limitations in video storage capacity, particles were continuously released into the flume over a period of 10 minutes. After this duration, the cameras were stopped, the footage was saved, and the cameras were turned on again for the next run. After the completion of three runs, the wave generator was switched off in order to stay within the programmed 45 minutes. The flume was then allowed to rest until a stable water level was reached again and the procedure could be performed again.

On average, a total of 15 particles were released in each run. The presented procedure was repeated until the desired number of particles fully travelled through the portion of the flume spanning from before the breaking location until the beaching point. Due to limited time availability at the wave flume facility, the desired number of trajectories to obtain within this campaign was set around 60-80 particles for every relative density step. However, the higher-density particles, particularly those with a relative density of 0.93, moved significantly more slowly than the lighter particles, resulting in fewer captured trajectories for these categories.

3.4. Hydrodynamic Conditions

To verify that the generated wave condition in the flume matched the intended settings and remained consistent throughout the experimental runs, the wave gauge data at Location 1 were analysed. The location of this wave gauge was selected because, at this location, the waves had not yet interacted with the slope. From this data, the initial spin-up time and the end of the time series-where the paddle was turned off and the water began to calm down-were excluded. Ensuring the accuracy of the generated wave heights was critical, as particle transport was analysed based on the intended wave characteristics; therefore, it was essential that the actual wave heights matched the intended wave heights settings. Additionally, verifying the stationarity of the wave condition was crucial, as non-stationary wave behaviour could lead to time-dependent variations in the particle trajectory dataset, as the particles were released one by one over time. The verification was done using two different approaches, both described below.

First of all, an analysis of the water surface elevation data was conducted using the zero-crossing method. This method identifies individual waves by locating the points where the water level crosses the mean (zero) line. The wave heights were calculated as the difference between the local crest and trough elevations for each detected wave. The data was then divided into consecutive 15-second blocks (10 waves per block). The average wave height across the blocks was compared to the programmed wave height and it was assessed if the measured wave height remained stable over time.

Secondly, on top of the first method to check stationarity an additional statistical test was performed. The Augmented Dickey-Fuller (ADF) test was applied to the wave height series extracted using the zero-crossing method. The null hypothesis of this test states that the time series has a unit root, implying non-stationarity, while the alternative hypothesis indicates stationarity (Plus 2023).

3.5. SWASH Model

In order to support the experimental work conducted in the wave flume, a numerical model was developed using SWASH. The following section aims to justify and explain how this was performed.

SWASH (Simulating WAves till SHore) is a wave-flow model designed to simulate unsteady, non-hydrostatic, free-surface, rotational flow and transport phenomena in coastal waters. Forcing such as waves, tides, buoyancy and wind can be simulated. It provides a general basis for describing wave transformations from deep to shallow water or even more complex scenarios such as harbours or ports. SWASH is capable of resolving short-wave dynamics such as wave breaking, swash, and overtopping, making it suitable for simulations in wave flumes. In flume research, SWASH can be used to replicate experimental conditions and validate physical measurements. This allows for testing various scenarios digitally before or alongside laboratory experiments in the actual flume.

Within this research, SWASH was used alongside the experiments in the actual flume to simulate the waves generated in the laboratory. The final goal of this analysis was to transition from discretised information about the wave dynamics limited to the locations in the flume where measuring instruments were installed, to a continuous set of data along the horizontal direction of the flume. The results obtained from the SWASH model were compared to the measured wave characteristics to ensure its reliability in representing the experimental conditions. This was achieved by comparing the surface elevation data collected by the six wave gauges installed along the flume (described in Section 3.1.3) to the results of the SWASH model in the exact same measuring locations. Good agreement between simulated and measured wave conditions at all six locations would indicate that the SWASH model reliably captures wave behaviour throughout the entire length of the flume. A more detailed description of the SWASH model design can be found in Appendix D.

The comparative analysis was based on four key hydrodynamic parameters, significant wave height (H_s), significant wave period (T_s), wave asymmetry (μ) and wave skewness (λ). These were computed starting from the surface elevation time series measured at the real and virtual wave gauges. First, the numerical model and the experimental data were compared using the variance density spectrum. This can show how the wave energy is dispersed throughout the various frequencies, making it a useful first indication of agreement between the model's outcome and the measured data. Beyond the spectral comparison, the above-mentioned wave parameters were used to assess the compliance between the modelled and measured conditions. To assess the agreement in shape of the simulated waves, the horizontal asymmetry (μ, asymmetry) and vertical asymmetry (λ, skewness) of the waves were computed and compared. These were computed respectively as 3.2 and 3.3 according to Myrhaug et al. (1986).

$$\mu = \frac{\eta'}{H} \tag{3.2}$$

Where:

- η' is the crest elevation above the mean water level [m],

- H is the wave height, i.e., the vertical distance from trough to crest [m].

$$\lambda = \frac{T''}{T'} \tag{3.3}$$

Where:

- T' is the time from the preceding zero-crossing to the crest [s],
- T'' is the time from the crest to the next zero-crossing [s].

The values of these parameters computed using the complete available surface elevation time series from the modelled and real wave gauges were compared by assessing the relative difference between them. If the difference of the values was considered small enough for all the computed parameters across the different wave gauges, the model could be considered representative of the experimental conditions inside the flume. Having a representative model results in a continuous data grid of the waves at each longitudinal location over time. This will help with determining the edges of the different wave zones (shoaling, breaking, surf and swash) and will allow local wave steepness calculations throughout these zones, which is of importance for further analysis.

3.6. Particles Drift

This section outlines the methodology used to extract MPD trajectories and assess their drift within the flume. This process entails a first step of transition from raw video footage to complete sets of x and y coordinates of particles' position over time using the software YOLO and validated with Tracker. The horizontal drift velocity of the MPD was then computed and compared with other theoretical speed values.

3.6.1. Preliminary Particle Drift Analysis

Initially, a preliminary analysis was conducted regarding the drift speed of each of the different categories to determine the best approach for further analysis. The results of this preliminary analysis are discussed in Appendix E. This analysis yielded that there are significant differences between different density categories, both in terms of total distance travelled and in the way particles from different categories behave across different wave zones.

3.6.2. Particles Detection: YOLO

In this research, YOLO was used to track the particles captured in the video recordings. YOLO (You Only Look Once) is a real-time object detection algorithm that identifies and localises objects within images or video frames (Melanie 2024). To tailor YOLO for this specific application, a training dataset is required. Roboflow was used to upload and label images, split datasets, and export them in the correct format for YOLO training. This process involved extracting frames from video footage and manually labelling the location and colour of each particle.

Once the dataset was prepared, the YOLO model was trained using Python, enabling it to recognise and track particles in new video frames. A Python script then processed each video, applying the YOLO algorithm to detect particles and record their (x, y) position for every frame. These coordinates were stored as text files in a specified output directory. The Python scripts can be found via a link shared in Appendix H.

To ensure accurate and efficient detection, the videos were pre-processed before being fed into YOLO. The following steps were taken:

1. The three overhead camera segments were synchronised using a beep sound audible in all recordings. As the cameras were started sequentially, this beep allowed the videos to be trimmed and aligned at a common t = 0 seconds.

2. Videos were rotated and cropped to include only the flume, with the origin of the reference frame in the bottom-left corner, and the other ends of the reference frames forming the top-left and bottom-right corners.
3. Compression was applied after confirming that YOLO maintained performance at lower quality, improving processing speed and storage efficiency.

These preprocessing steps ensured that the videos were ready for accurate particle tracking using the trained YOLO model.

3.6.3. Tracking Algorithm

This section presents the overall workflow of the tracking algorithm, including the YOLO detection data and all the steps involved in extracting, processing, and analysing particle trajectories. This is initiated from YOLO detection outputs and provides as an output a structured dictionary of particle trajectories for further analysis.

The complete tracking algorithm was developed in Python and was organised in five main components: parameter configuration, detection and tracking, detection processing, trajectory merging and final data organisation. Each part is stored in dedicated scripts which are available in a GitHub repository along with a thorough documentation of every function used which can be found in Appendix H.

The first step consists of the configuration of all relevant settings and parameters. These are video-specific information and a set of thresholds defined to guide the processing and merging of the trajectories. More on the definition of these thresholds can be found directly in the code documentation.

With all the settings and processing thresholds established, the next phase consists of the actual tracking. Particle detection is done by feeding the preprocessed videos to a YOLO-based model. In this step, single particles in the videos are tracked over time. This results in raw label data consisting of x and y coordinates for every detected particle for every frame of the video. The label data is read and processed to organise the obtained detections into single trajectory pieces. This is done by splitting the data into segments based on the proximity of the detections in both space and time using defined thresholds for maximum frame and positional gaps. Any potential errors in the tracking process are filtered out by only considering segments with a sufficient number of tracked locations.

Given that each experimental run was recorded from multiple top-view cameras, a merging process was included to be able to reconstruct complete particle trajectories. The obtained partial trajectories of the same particle across different viewpoints were aligned and combined. This was handled by comparing the position, timing and colour of the particles, ensuring accurate merging into continuous paths.

The processed and merged trajectories were finally compiled into a dictionary which includes the whole set of particle trajectories in real-world coordinates together with the related metadata for each experimental run. Trajectories corresponding to specific runs or experimental conditions can be accessed based on the wave height, the run identification number and the particle's weight. This allows for further analysis and comparison across the different particle types and experimental runs.

3.6.4. Trajectory Validation with Tracker

Tracker is a free, open-source video analysis tool developed by Open Source Physics that allows users to track and analyse object motion in videos. In this research, Tracker was used to generate reference trajectories by combining its auto-tracking feature with manual corrections when the particle was lost. Real-world distances were determined using the same reference frame setup as in the YOLO-based tracking. By closely supervising the tracking process, it was ensured that the resulting trajectories were reliable, which were then used to validate the automated YOLO tracking. Additionally, Tracker was used to track the wave crests, to obtain crest speed values.

3.6.5. Trajectory Processing

The trajectory data along the flume showed oscillations caused by particle-wave interactions. However, this research focuses primarily on the net drift of the particle, rather than its instantaneous back-and-forth motion.

To be able to estimate the net drift speed along the full trajectories the existing gaps in data resulting from the tracking process were filled. This was done by applying a 1D linear interpolation of the x-position data as a function of time. The level of completeness of the trajectory data was satisfactory to yield good results after interpolation. The interpolated data showed perfect agreement with the initial trajectories and allowed for continuous data to be obtained along the horizontal direction.

In order to capture the actual net horizontal drift speed, a Butterworth low-pass filter was applied to the interpolated trajectories to remove high frequencies from the particles' motion. This resulted in a smoothed signal, which allowed for the estimation of the net drift of the particles.

The filtered trajectories were segmented based on a step distance of 0.2 metres. For each segment, the particle velocity was estimated by dividing the horizontal displacement by the relevant time interval. The speed values of all trajectories were grouped per bin, and the mean and uncertainty were calculated to obtain average drift speeds for each relative density category for every 0.2 metres along the length of the flume.

3.7. Computation of Wave Propagation speeds

The wave motion observed in the experiments was characterised by computing key wave propagation parameters: the wave phase speed, the wave crest speed and the Stokes drift. These provide insights on the different wave speed components and were compared to the particles' drift to assess their relation to the MPD transport. The following sections describe the computational approaches used for every parameter.

3.7.1. Phase Speed

As mentioned in 2.4.1, phase speed describes the speed at which the wave is propagating, which depends on wavelength and period. In this research, the phase speed was determined assuming linear waves, using formula 2.14 and determined with the additional corrections for non-linearity using formula 2.15. Both formulas require wave height (either directly or via the wave number k and wavelength L) and water depth as inputs. Since both the mean wave height and the water depth change along the length of the flume due to the presence of the slope, local phase speed values for 0.2 metres segments along the length of the flume were determined. Within each 0.2 metres segment, the mean still water depth and mean wave height-determined by SWASH-were estimated as constant over the narrow segment.

3.7.2. Crest Speed

Crest speed is the speed at which the highest point of a wave travels through the water. As mentioned in section 2.4.1 it should be the same or similar to the phase speed. Within this research the crest speed was determined using the SWASH model and the zero-crossing method. For each 0.2-metre segment along the flume, the time at which a specific wave crest passed was recorded at two consecutive points. By calculating the time difference between these two points and dividing the known distance of 0.2 metres by this time difference, the local crest speed was determined for each segment. Repeating this process for approximately 700 waves provided robust estimates of the crest speed.

Additionally, a second method to estimate the crest speed was applied using the top-view video recordings and Tracker. In this approach, the crest of each wave was manually tracked over the first 5.5 metres after the particle release location by marking its position frame by frame for approximately 15 waves. The speed values determined were averaged again over 0.2 metres segments, to allow direct comparison with the crest speed values determined using SWASH.

3.7.3. Stokes Drift

In this specific application the Stokes drift was locally determined along the longitudinal direction of the flume. The presence of a sloped bottom made the estimation of local drift values necessary as the water level, and consequently local steepness, was variable along the flume.

Values for Stokes drift were therefore computed every 0.2 metres along the whole length of the flume. This was made possible by the results of the SWASH model which provided surface elevation time series for every x-location.

A 0.2 metre discretisation was selected to ensure precise representation of the Stokes drift variability across the slope.

Legend: ▬ 100% overlap ▬ 90% overlap with minimal adjustments ▬ 0% overlap

4

Results

This chapter provides an overview of the results of the laboratory experiments conducted to investigate the influence of particle density on the horizontal transport and beaching behaviour of Marine Plastic Debris. To address this research question, the experimental setup is first validated. Subsequently, the particle drift is analysed, and lastly, the observed particle drift values are compared to wave propagation speeds to assess how changes in particle density influence transport within the given waves.

4.1. Overview Experimental Runs

A total of seven different particle density categories were used during the experimental campaign. As previously mentioned, all particles started at the same location in the shoaling zone in the flume, which was located 19.5 metres from the wave maker (further referred to as $x_p = 0$ m). The particles continued their movement until stabilising on the beach, which occurred within a spread of approximately 1 metre—between 26 and 27 metres along the flume—corresponding to $x_p = 6.5–7.5$ metres.

Table 4.1 shows the number of trajectories obtained for each particle density category gathered in the experimental campaign.

Particle Weight (PW) [g]	**Relative Density (RD) [-]**	**Number of Trajectories (Full Length Dataset, 0–7.5 m)**	**Number of Trajectories (Initial Section Dataset, 0–5 m)**
3	0.09	71	90
5	0.15	69	85
7	0.23	59	92
13	0.42	29	47
23	0.69	25	47
25	0.75	36	65
32	0.93	5	10

Table 4.1: Overview of particle characteristics and the number of usable trajectories captured from merged video segments. The full flume trajectories (0–7.5 m) are based on merges of three camera views, while the initial flume trajectories (0–5 m) are based on merges of only two views.

The variation in the number of trajectories across categories can be attributed to several factors. Firstly, differences in particle density led to variations in drift speed along the flume. As a result, within a fixed time window, slower-moving particles crossed the flume less frequently than their faster counterparts. Furthermore, initial assessments of travel velocity data suggested greater variability in the trajectories of lighter particles. To address this, a larger number of lighter particles were released during the experiments to improve statistical representation.

In addition, the YOLO model exhibited varying levels of performance across different trajectories, in which some particles were not being tracked consistently enough to gain usable data. Moreover, trajectories were lost during the data processing phase. While the YOLO model shows high classification accuracy for individual particles (92–93%), it also demonstrates a tendency to misclassify background pixels as particles (For more details see Appendix G), adding to the complexity of processing the data. In addition, as detailed in Section 3.6.3, the merging of trajectory segments relied on temporal and spatial alignment, based on a loud sound cue and manually measured reference frames. These steps introduced a degree of human error, which in some cases led to poor alignment and caused certain trajectories to be excluded from the final dataset. This explains why, as shown in Table 3.6.3, the number of trajectories is higher when only two videos were merged (covering the first 5 metres of the flume) compared to when three videos were merged (covering the full 7.5 metres). The increased complexity and potential for misalignment when merging three videos led to more trajectories being discarded during processing. Both sets of trajectories—those from two-video merges and those from three-video merges—are used throughout the results section, depending on the specific location along the x-axis being analysed. It is noted for every figure whether the Full Length dataset or the Initial Section Dataset is used. The quality of the trajectories in each dataset was validated by comparing sample trajectories tracked with YOLO to the same particle paths tracked using Tracker. The comparison showed good agreement, the result of which is added in Appendix F, confirming reliable performance across the datasets.

Each dataset includes a number of particles that interact with the glass wall. Particles are released in the middle of the flume (in the y-direction) but tend to drift towards the glass side walls throughout their journey to the beach. To preserve the statistical robustness of the analysis, all particle trajectories—whether they interact with the sidewalls or not—were retained in the dataset. However, sidewall interactions are expected to affect the drift patterns of the particles, potentially affecting for example their net forward drift speeds. This influence is not quantitatively accounted for in the results presented in this research. Figure 4.1 shows for one metre segments along the flume the percentage of particles in that category that interact with the glass side walls at any moment in time within that segment.

In this analysis presented in Figure 4.1, the flume was divided into one-metre segments along the x-direction. For each segment, the percentage of particles per category that touched the glass side walls (defined as a y-position ≤ 0.05 metres or ≥ 0.75 metres) at any moment during their presence in that segment was calculated. A particle was counted only once per segment, regardless of how long or how often it interacted with the wall within that segment. Importantly, this method does not track cumulative or continuous interactions across segments but assesses each segment independently.

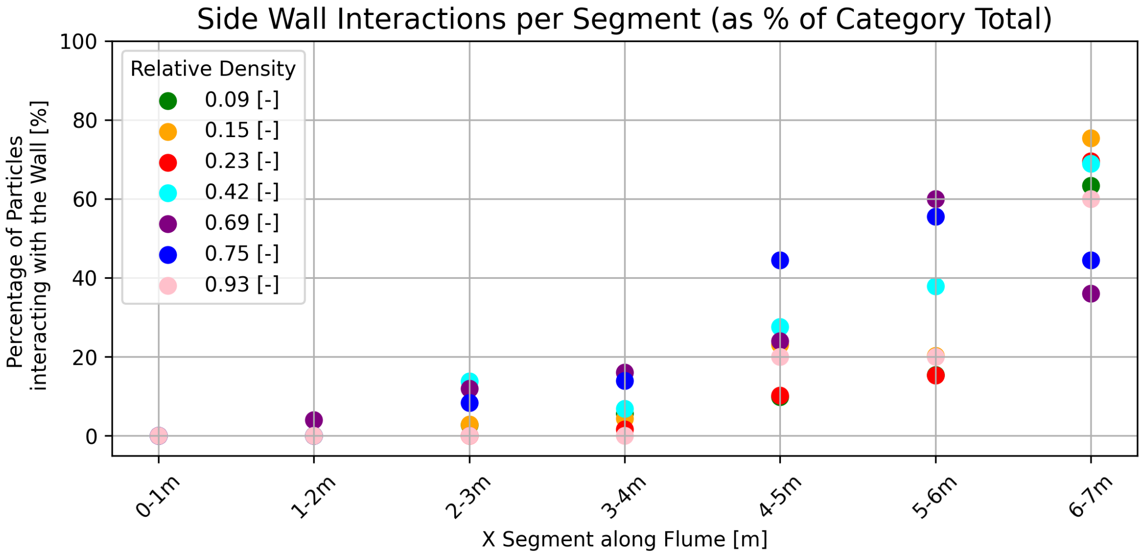

Figure 4.1: The percentage of particles per category that touched the glass side walls (defined as a y-position ≤ 0.05 metres or ≥ 0.75 metres) at any moment during their presence in the segment (Made using Full Length Dataset).

Figure 4.1 shows that sidewall interaction increases along the flume. Early interactions are limited due to the placement in the middle of the cross-section. As the particles slow down further down the flume, they spend more time per segment, increasing the chance of drifting sideways and hitting the walls. In the final metres of the flume, wave fronts are no longer perfectly perpendicular to the glass walls. Instead, they approach the beach at an angle, estimated up to 25 degrees. At times, the centre of the wave moves faster than the sides, creating a forward-curved shape, while at other times, the sides advance more quickly, forming a reversed curve. These wave asymmetries vary over time and do not appear to follow a consistent pattern. Although no formal bias analysis was conducted, this angled wave approach likely enhances sideways particle movement, contributing to the increased wall interaction observed in the later flume segments. Interpreting the results presented below, it should be considered that there is an increasing percentage of interaction further down the flume, making the results near the end less reliable than the results in the initial segments.

4.2. Hydrodynamic Conditions and Wave Characteristics

4.2.1. Generated vs Input Waves and Wave Uniformity

The block-wise analysis of the wave elevation data, based on the zero-crossing method, yielded average wave heights ranging between 0.1081 metres and 0.1097 metres across the measurement period. These values are slightly below the programmed wave height of 0.110 metres. However, the overall mean of 0.109 metres closely approximates the programmed value. Given the millimetre-scale differences and the experimental tolerances in wave flume settings, this deviation in mean wave height is considered negligible in practical terms. Within each block, the standard deviation of wave heights remained consistently low, with a maximum observed value of 0.00068 metres. These results indicate minimal variability within individual blocks and show an initial indication of the absence of temporal evolution of wave height throughout the experimental run.

The p-value of the Augmented Dickey-Fuller (ADF) test was 0.003, which is below the 0.05 threshold set within this research, allowing the null hypothesis to be rejected. This confirmed that the wave height series was statistically stationary, meaning its mean and variance remained constant over time, thereby supporting the assumption of steady-state wave conditions during the experimental runs.

The methods above confirmed that the wave height remained stable and consistent over time, with only millimetre-scale deviations from the programmed value, thereby validating the reliability of the generated wave condition.

4.2.2. SWASH Validation

To determine the wave propagation properties for the wave condition used in the experimental setup, a continuous profile of the wave height is required. Due to the limited number of wave gauges installed in the flume, the wave height profile along the flume was obtained using the SWASH model, as described in detail in section 3.5.

To validate the SWASH model, it was first assessed whether both the simulated and observed wave signals exhibit similar spectral characteristics. Figure 4.2 shows the wave energy spectra for each wave gauge location for both the measured data and the simulated data. Each curve represents the energy distribution across different frequencies. A vertical dashed line at 2/3 Hz highlights the expected dominant frequency, since it represents the input period of 1.5 seconds. The consistency of the spectral peaks around this frequency across all locations confirms that the wave signals retain the intended frequency content as they propagate through the flume. Smaller peaks are visible at superior harmonics of the main frequency, which can be attributed to non-linear aspects of the waves due to for example reflection, however, they remain almost two orders of magnitude lower than the main peak.

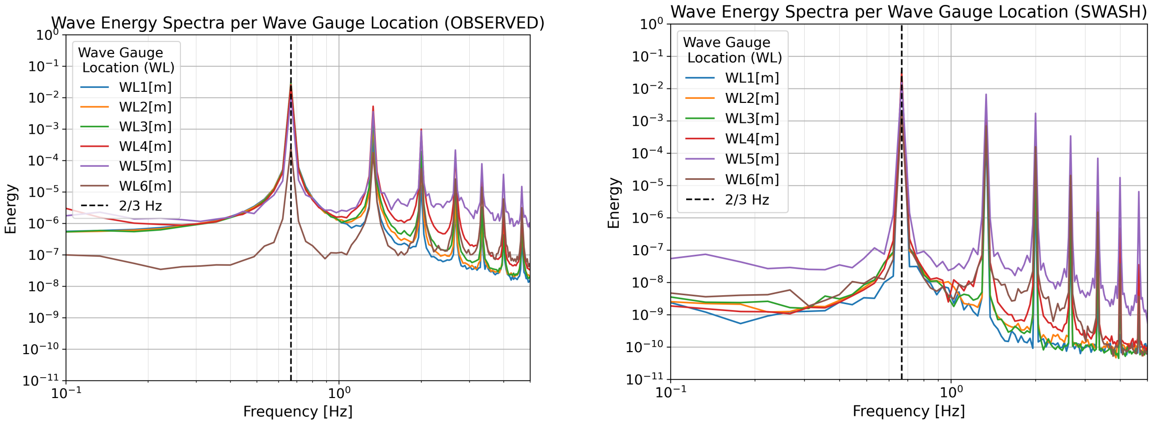

(a) Wave energy spectra at each wave gauge based on measurements.

(b) Wave energy spectra at each wave gauge from SWASH simulation.

Figure 4.2: Comparison of wave energy spectra from wave gauge measurements and SWASH simulations.

The simulated wave heights were compared with the measured wave heights at corresponding locations within the flume. Table 4.2 presents the modelled and measured mean wave heights, each averaged over a large number of waves, along with the corresponding standard deviations for both sets of mean values.

Wave Gauge Number	**Location [m]**	**Observed Mean Wave Height [m]**	**Std. Dev. Observed [m]**	**Simulated Mean Wave Height [m]**	**Std. Dev. Simulated [m]**
1	x_f = 5.0	0.109	0.0006	0.110	0.0009
2	x_f = 13.0	0.108	0.0006	0.110	0.0007
3	x_f = 14.3	0.109	0.0008	0.109	0.0007
4	x_f = 18.2	0.122	0.0096	0.120	0.0004
5	x_f = 21.5	0.087	0.0072	0.108	0.0060
6	26.0	0.013	0.0078	0.036	0.0002

Table 4.2: Comparison of modelled (SWASH) and observed (Wave Gauge) mean wave heights, averaged over multiple waves at different locations along the flume. The flume's origin is set at $x_f = 0$ metre. (Wave breakpoint is at x_f = 21 metre.

Table 4.2 shows that SWASH successfully simulates the observed wave heights, with differences typically within one to two millimetres. Statistically, the low standard deviations suggest that the differences in simulated and observed mean wave heights at the first four locations are significant. However, from a practical perspective, these small deviations—on the order of millimetres—can be considered negligible. This indicates that the SWASH model reliably simulates the generated waves up to the shoaling zone. Between locations 4 and 5, the waves begin to break. After this breaking point, at wave gauges 5 and 6, the differences between the simulated and observed wave heights become more pronounced. The SWASH model overestimates the wave heights at both locations: at location 5, the simulated wave height is approximately 24 % higher than the observed value. At the far end of the flume, at location 6, SWASH predicts a wave height nearly three times greater than what was measured. However, it is important to note that location 6 lies far up the slope, where measurement accuracy may be reduced due to instrument limitations.

These results suggest that while SWASH performs well in simulating wave propagation before breaking, it tends to overestimate wave heights in the breaking and particularly the swash zone. Nonetheless, the overall performance of the model remains relatively strong and is used to estimate the wave heights along the length of the flume throughout the rest of this research.

4.3. SWASH Simulation

Once the SWASH model is validated against observed data, it can be used to generate a continuous wave height profile along the length of the flume. The resulting profile is shown in Figure 4.3. This figure shows the mean wave height throughout the flume.

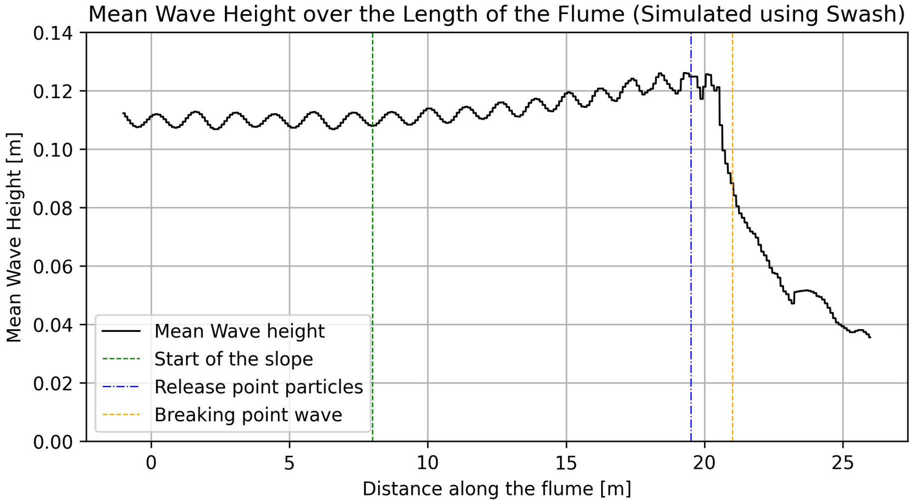

Figure 4.3: Mean Wave Height over the length of the flume (simulated by SWASH)

It can be seen that there is a periodic oscillation in the mean wave height values. These oscillations is likely due to the reflection of the waves in the flume. As the waves travel down the flume and encounter boundaries such as the slope or the end wall, a portion of the wave energy is reflected back toward the wave maker. This reflected energy interacts with the incoming waves, producing wave patterns other than the intended wave patterns due to constructive or destructive interference along the flume.

Figure 4.3 also shows the evolution of wave height as the wave propagates along the flume and interacts with the sloping bathymetry. Initially, as the wave travels in the deeper section of the flume (up until x_f = 8 metres), the wave height remains relatively constant. However, once the wave begins to interact with the slope (beyond x_f= 8 metres), the shoaling process starts, causing the wave height and steepness to increase. This growth in wave height through the shoaling zone aligns with theoretical expectations and confirms that the model captures this key mechanism. As the wave continues to move shoreward and the depth becomes shallower and the wave steepness increases further, it reaches a critical point where it becomes unstable and breaks. This breaking point is characterised by a sudden decrease in wave height (x_f = 21 metres), as a significant portion of the wave's energy is dissipated through turbulence and the generation of higher-frequency motions. Beyond the breaking point, in the surf zone, the wave height continues to decrease gradually due to ongoing energy dissipation from turbulence and bottom friction. The profile thus reflects the full wave transformation process—from shoaling to breaking to post-breaking dissipation.

4.4. Particle Transport

This section presents particle drift speed along the flume, starting with the full near-coastal zone (shoaling to beaching), followed by a detailed look at specific wave transformation zones.

4.4.1. Particle Transport over Full Length

To answer the research question regarding the effect of density on the beaching behaviour of the particles near the coast, the location data of the particles was first assessed in the direction along the flume. The notation x_f refers to distances from the wave maker. Distances from the particle release point are denoted as x_p, with $x_p = 0$ metres corresponding to the particle release point, which is consistently at $x_f = 19.5$ metres.

Figure 4.4b presents the mean net drift speed in the x-direction for each density category, measured over the full transport distance from the release point at $x_p = 0$ metres to the end of the surf zone at $x_p = 6.5$ metres. The results show a gradual decrease in transport speed with increasing particle density, allowing for the fitting of a linear and an exponential trend line.

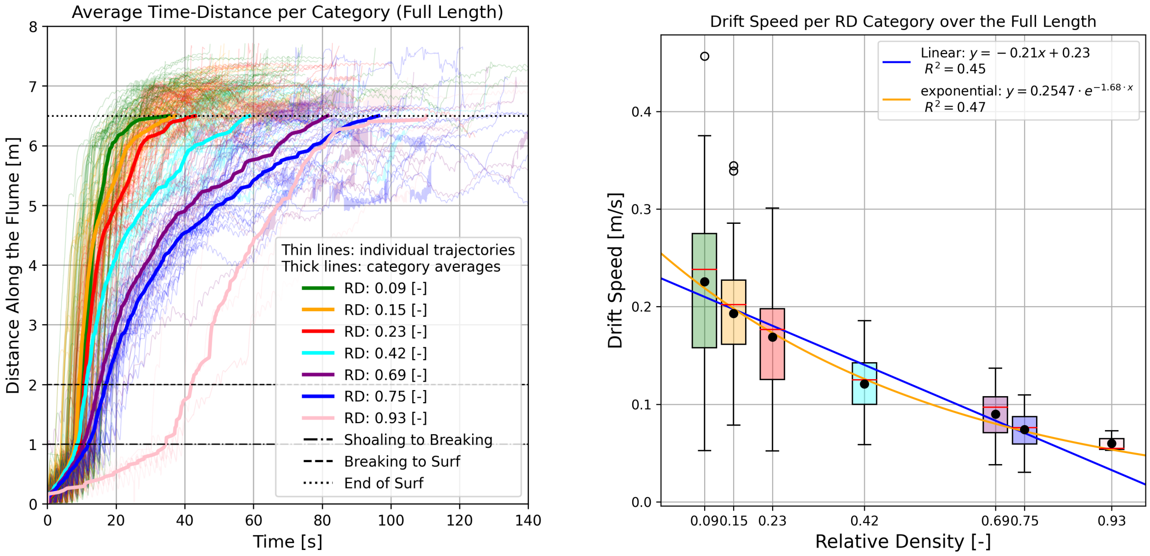

(a) Travel distance along the flume ($x_p = 0$ until $x_p = 6.5$ metres) over time. Thin lines show individual particle trajectories; thick lines represent the average trajectory per category.

(b) Mean net horizontal drift over distance from x_p = 0 [m] until x_p = 6.5 [m] for each density category.

Figure 4.4: Particle drift speed assessed over full length of the flume (Made using Full Length dataset).

The particle drift along the length of the flume for the different categories is displayed in Figure 4.5. This figure shows the mean local drift speed over segments of 0.1 metres along the length of the flume for each different density category, with whiskers to indicate the uncertainty of each point. It can be seen that there is a significant difference in drift for the different categories around the breaking point, with speeds ranging approximately from 0.4 to 1.5 metres per second. Eventually, all drift values reduce to almost zero near the end of the flume, where a strong decrease is seen as soon as particles start to interact with the slope.

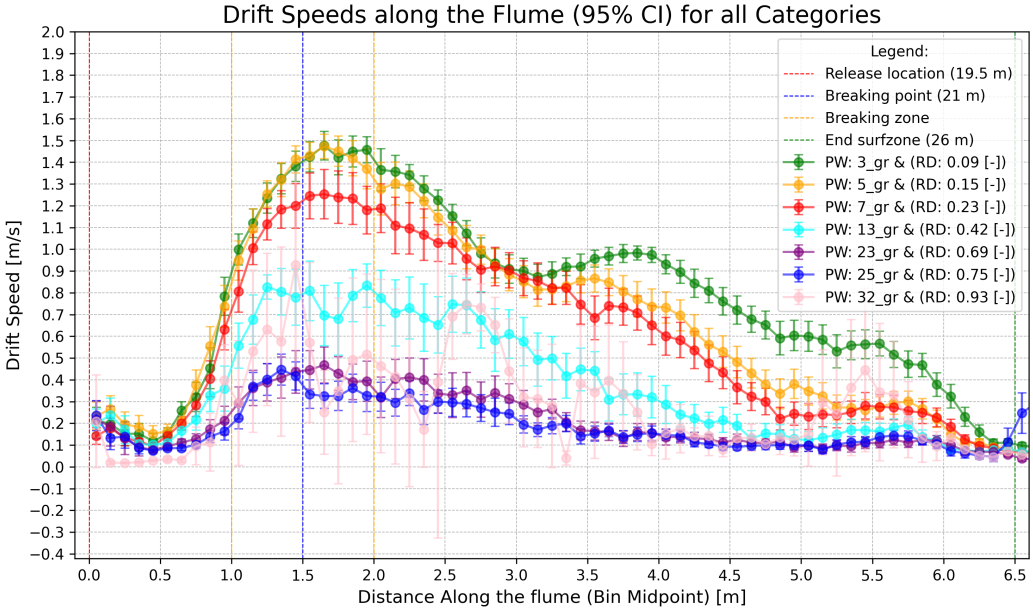

Figure 4.5: Mean drift values in x-direction averaged over 0.1 [m] segments for all trajectories within each category (Made using Full Length dataset).

4.4.2. Particle transport in the Shoaling zone

Zooming in more specifically on the shoaling zone, Figure 4.6a reveals that throughout the shoaling zone, the slopes of the average trajectory lines for each category are similar for all categories except the particle with a relative density of 0.93 [-]. This is also reflected in Figure 4.6b, which shows the mean drift speed for each category over the distance between $x_p = 0$ metres and $x_p = 1$ metres, showing mainly drift values around 0.12 metres per second for all density categories except the highest density one. It is important to note that while the averages for most categories are based on at least 47 trajectories or more, the 0.93 category is based on only 10 trajectories. As a result, the average for this category is subject to greater variability and should be interpreted with caution. The trend lines in Figure 4.6b both fit poorly, indicated by the low R^2 value. This suggests that there is no significant relationship between particle density and drift speed in the shoaling zone.

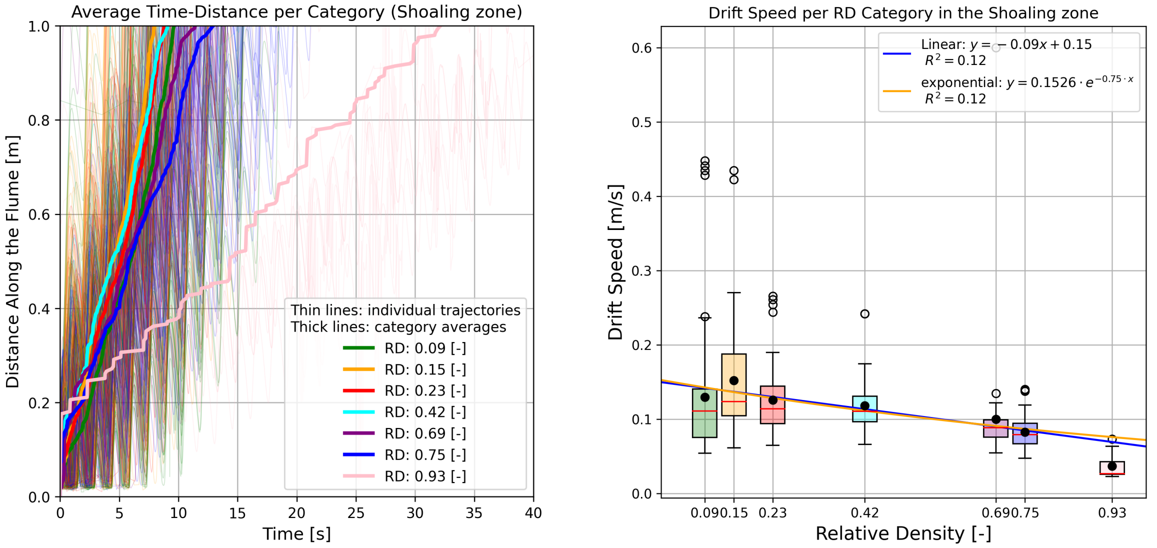

(a) Shows how particles move through the first metre in the x-direction over time, corresponding to the shoaling zone. Thin lines show individual particle trajectories; thick lines represent the average trajectory per category.

(b) Drift speed over distance from x_p = 0.2 [m] until x_p = 0.7 [m], which is the shoaling zone, for each density category

Figure 4.6: Particle drift speed assessed over the shoaling zone (Made using Initial Section Dataset).

4.4.3. Particle transport in the Breaking zone

The breaking zone is determined to lie between x_p = 1 and x_p = 2 metres, and can be described as the transitional region between the shoaling and surfing zones. A more detailed display of the trajectories through this zone is shown in Figure 4.7a. In this figure it can be seen that around x_p = 1 metre, there appears to be a tipping point where particles experience a sudden increase in speed, indicating the beginning of the breaking zone. Moreover, it can be seen that the slopes of the lines vary more strongly between different categories, suggesting a deviation in travel speed throughout the different categories. Rather than a sudden or stepwise change in speed between the lower-density categories (e.g., 0.09 and 0.75), there is a gradual decrease in velocity as density increases. Notably, the 0.93 density category deviates more significantly from the others. Particles in this category appear to remain in the shoaling zone for a longer period, reaching the tipping point around x_p = 1 metre more slowly. However, once this point is reached, they also exhibit an acceleration. This delayed but rapid response suggests that the 0.93 category interacts differently with the flow conditions, possibly due to its closer proximity to neutral buoyancy. However, once again, it is important to note that only 10 particles were assessed within category 0.93 [-], which is relatively low.

Figure 4.8b shows the box plots of the drift speed values found in this zone. This figure shows a progressively steeper increase across the different categories. The least-squares linear regression results in a negative drift speed on the high relative density side of the range. While it helps illustrate how drift decreases with increasing density, the extrapolated negative values are not physically meaningful. The limits of the linear fit justify the consideration of alternative models (such as exponential fits) that asymptotically approach zero without violating physical constraints.

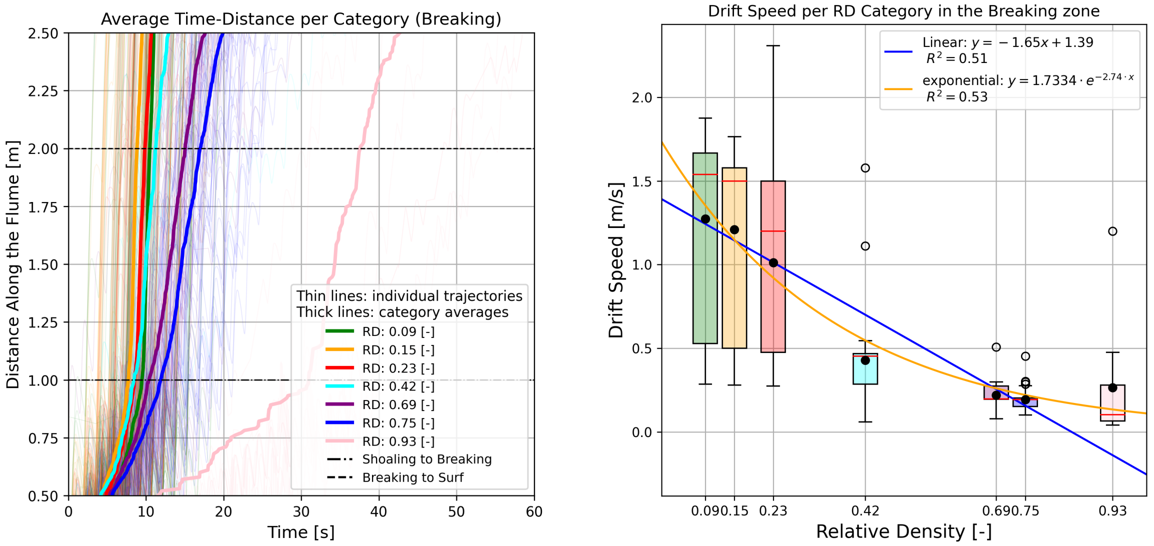

(a) Shows how particles move through x_p = 0.5 - 2.5 metres in the x-direction, corresponding to the end of the Shoaling zone and the beginning of the Surf zone, in which breaking represents the transition between these two zones. Thin lines show individual particle trajectories; thick lines represent the average trajectory per category.

(b) Drift speed over distance from x_p = 1 [m] until x_p = 2 [m], which is the breaking zone, for each density category (Made using Initial Section Dataset).

Figure 4.7: Particle drift speed assessed over the breaking zone (Made using Initial Section Dataset).

4.4.4. Particle transport in the Surf zone

In the surf zone, detailed in Figure 4.8, drift speeds initially differ between categories due to acceleration through the breaking zone. Toward the end of the surf zone, all categories show a slowdown, reflected in the decreasing slope of their drift speeds. Notably, a substantial number of particles interact with the glass sidewalls in this zone across all categories, likely affecting drift speeds and representing a key source of uncertainty.

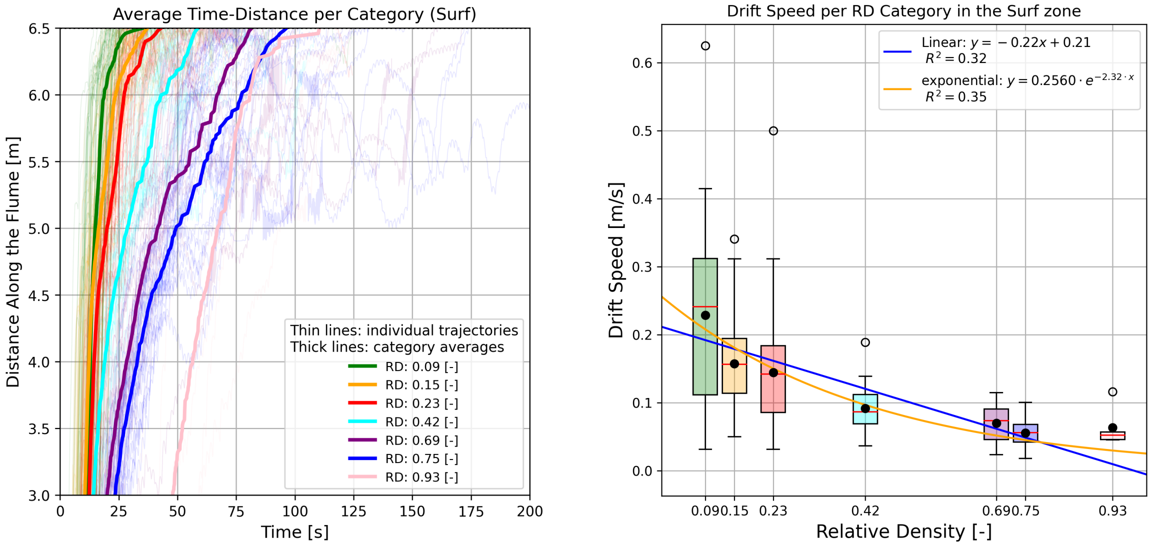

(a) Shows how particles move through x_p = 3 - 6.5 metres in the x-direction, representing the surf zone. Thin lines show individual particle trajectories; thick lines represent the average trajectory per category.

(b) Drift speed over distance in the surf zone which goes from x_p = 3 [m] until x_p = 6.5 [m] for each density category.

Figure 4.8: Particle drift speed assessed over the surf zone (Made using Full Length Dataset).

4.5. Wave Propagation Speeds

Wave propagation speeds, such as Stokes, crest, and phase speed, represent different aspects of how energy and motion are transmitted through water by waves. Comparing these to particle drift helps determine how closely particle movement follows wave-induced flow.

4.5.1. Stokes drift

The Stokes drift values along the flume were estimated using the mean wave height values obtained from the SWASH model. Figure 4.9 displays the resulting Stokes drift profile alongside the corresponding estimated wave height values. The Stokes drift estimates appear irregular near the breaking point, which can be attributed to the limitations of SWASH in accurately simulating wave breaking as it is visible that the wave height values estimated around the breaking point are also irregular.

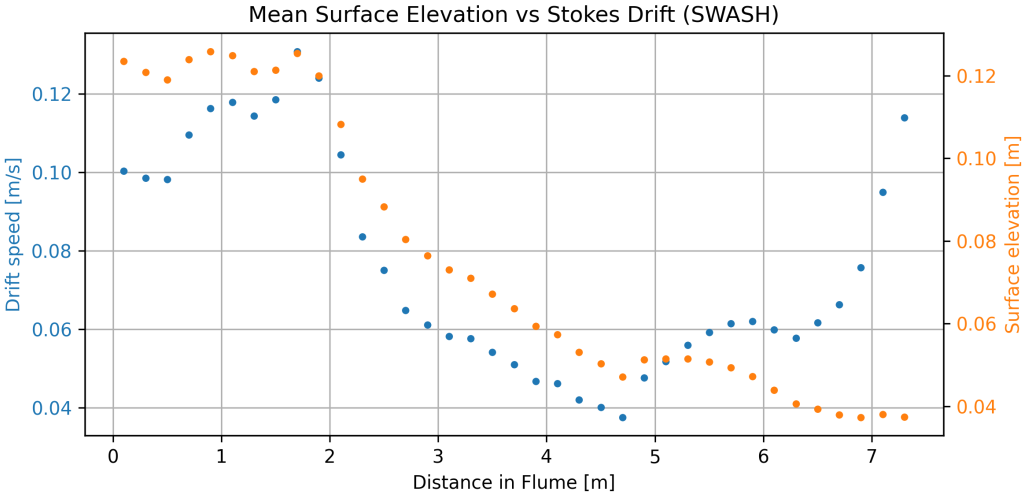

Figure 4.9: Estimated Stokes drift and estimated mean wave height values along the length of the flume.

Several sources of uncertainty influence the accuracy of the Stokes drift estimates. First of all, as mentioned above, the surface elevation and wave height values used as input are derived from numerical simulations and inherently carry model uncertainty, as discussed in the SWASH validation section. Second, the mean wave height values used in the calculations represent averages over a large number of simulated waves. However, this uncertainty due to averaging over waves was determined to be negligible. Lastly, the theoretical formulation for Stokes drift is less applicable beyond the breaking point, as it assumes non-breaking, regular wave conditions. This further limits the reliability of the estimates in the surf zone.

4.5.2. Crest Speed

The crest speed was determined using the simulated surface elevation data and by manually tracking a number of waves on the video material from the experimental campaign. The results of the comparison are displayed in Figure 4.10.

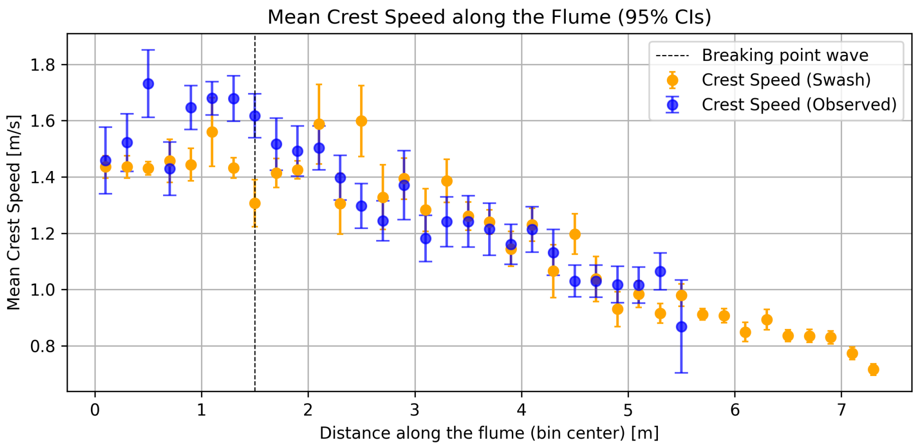

Figure 4.10: Crest speed estimations throughout the flume using simulated and observed data

It can be seen that the simulated and measured crest speed values align well considering the confidence bounds, especially throughout the surf zone. However, greater discrepancies are observed near the breaking point. These differences may be explained by the reduced accuracy of SWASH in the breaking zone, whereas manual tracking may better capture the actual crest speed in this region. However, the manually tracked mean values also carry uncertainty due to the small sample size and the potential for human error during tracking. Additionally, both methods share a common source of uncertainty from spatial averaging over a 0.2-metre domain. Despite these limitations, the strong agreement between both methods suggests that the estimated crest speed is reliable.

4.5.3. Phase Speed

The phase speed along the flume was also determined using two theoretical approaches based on mean have height values obtained from the SWASH model. The first approach assumes linear wave theory and the other includes the non-linear corrections. The results are shown in Figure 4.11.

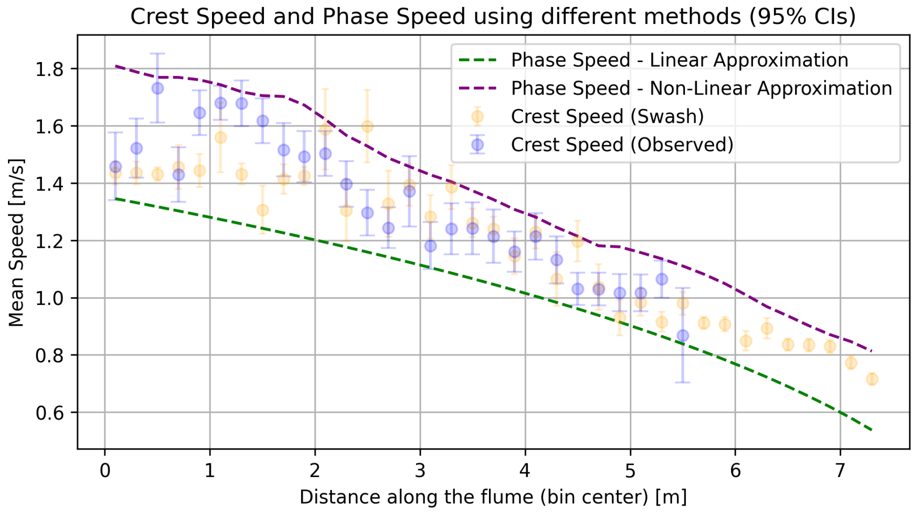

Figure 4.11: Phase speed along the flume based on linear wave theory and non-linear correction. Additionally, crest speed displayed as reference.

The crest speed and phase speed are expected to be very similar to each other. In the results, the linear and non-linear phase speed estimates closely bracket the measured crest speeds, all falling within approximately 0.2 m/s of each other. As seen in the figure, the linear phase speed estimates lie consistently below both the crest speed and the non-linear phase speed estimates. This is expected, as linear theory tends to underestimate phase speed in regions where wave non-linearity becomes significant, particularly in shallower water. The non-linear phase speed, which includes corrections based on wave height and water depth, provides higher values that seem to overestimate the crest speed measurements throughout the flume. To account for uncertainty in estimating crest and phase speed, this research uses the range between the linear and non-linear phase speed estimates as a confidence interval.

4.6. Particle Transport vs. Wave propagation Speeds

Figure 4.12 presents both the particle drift speeds and the wave propagation speeds in a single plot. It shows that particles across all density categories generally follow the Stokes drift velocity in the shoaling zone. However, as they approach the breaking zone the drift speeds begin to increase, indicating an acceleration likely caused by enhanced wave-particle interactions in this region.

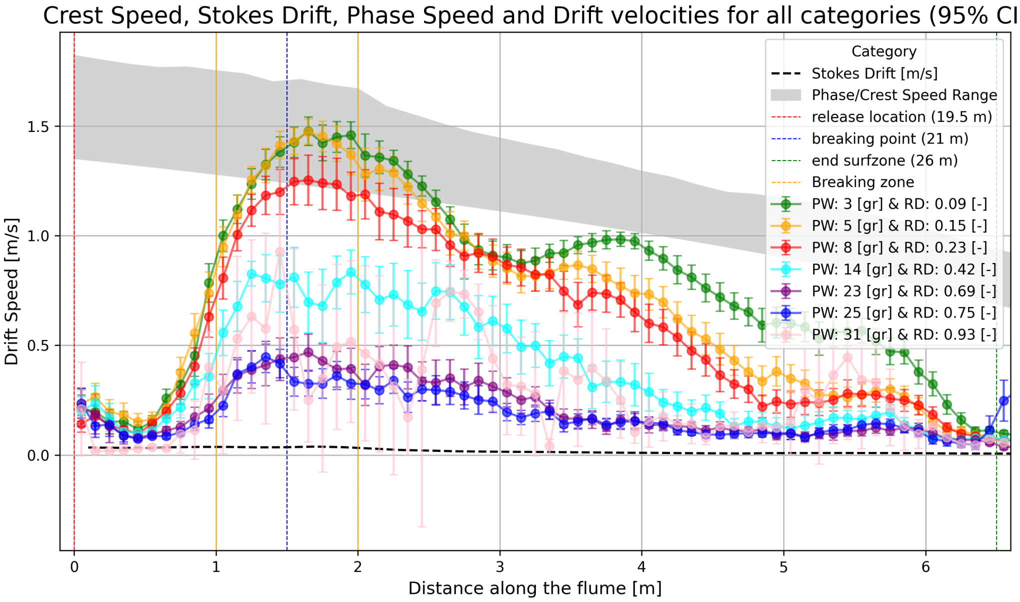

Figure 4.12: Stokes drift, Phase speed and crest speed and mean particle drift values along the flume (Made using Full Length dataset).

Figure 4.12 shows all particles starting out with a similar drift speed, which is very close to the estimated local Stokes drift. This link is further highlighted in Figure 4.13a

Additionally, Figure 4.12 shows that the lower the relative density of a particle, the higher its drift speed within the breaking zone. The lightest particles, with the lowest relative density, reach speeds comparable to the local wave phase and crest speed. This suggests that these particles may be surfing the wave crest over a distance of approximately 0.5 to 1.5 metres within the breaking zone, carried forward by the strong forward motion of breaking waves. These observations are further emphasised in Figure 4.13b.

Beyond this point, in the surf zone, the average drift speed begins to gradually decrease. This suggests that the particles are moved forward less and less by each passing wave as they move further onto the slope, which can be attributed to the dissipation of energy of the waves as they move over the increasing slope. As the wave loses energy, it imparts less momentum to the particles, reducing their net forward drift. Figure 4.13c highlights the surf zone and the link with the wave propagation speeds further.

Near the end of the surf zone, a sharp decrease can be seen. This likely corresponds to direct interaction between the particle and the sloping bed surface. As the bottom of the particle contacts the wooden slope, frictional forces increase, which further decelerate the particle and reduce its forward progression.

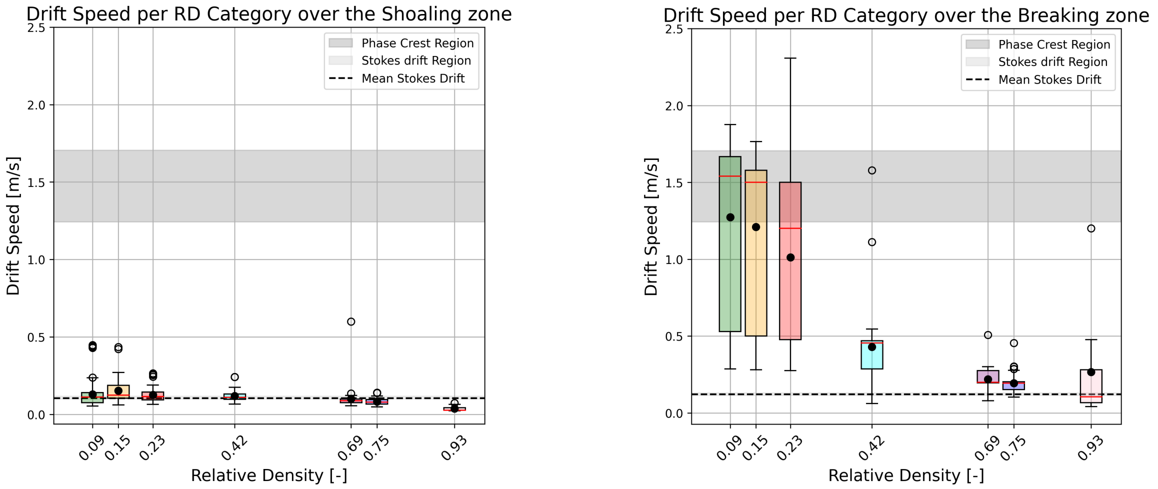

(a) Particle drift speed vs. wave propagation speeds in the Shoaling zone (Initial Section Dataset)

(b) Particle drift speed vs. wave propagation speeds in the Breaking zone (Initial Section Dataset)

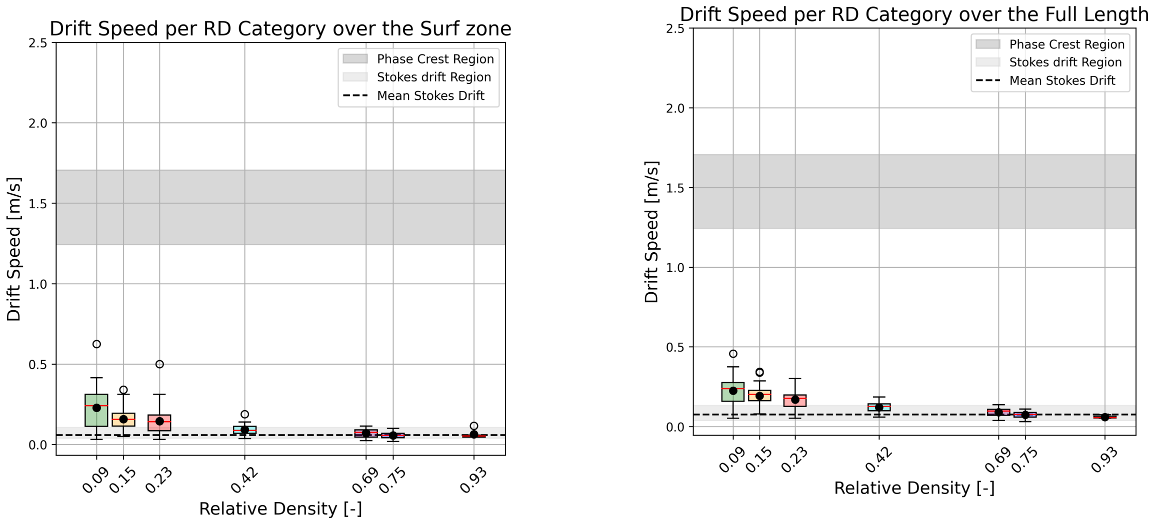

(c) Particle drift speed vs. wave propagation speeds in the Surf zone (Full Length Dataset)

(d) Particle drift speed vs. wave propagation speeds over the full length of the flume (all other three zones combined) (Full Length Dataset)

Figure 4.13: Particle drift speed compared to wave propagation speeds across different flume zones.

Legend: ▬ 100% overlap ▬ 90% overlap with minimal adjustments ▬ 0% overlap

5

Discussion

In the following sections, the results are interpreted with respect to the research objectives of this study and the existing literature. This research aimed to understand the effect of particle density on the horizontal transport and beaching behaviour of marine plastic debris. The horizontal particle movement was analysed by measuring net longitudinal drift.

A flume setup was used to generate regular waves with an offshore wave height of 0.11 metres and a period of 1.5 seconds. The waves propagated over a sloped bed with a 1:40 gradient. Particles with a density relative to water ranging from 0.09 to 0.93 were released in the shoaling zone just before the breaking point and were considered to be beached once they came to rest on the slope surface, typically within a span of approximately 7 metres from the point of release.

To answer the research question and subsequent sub-questions, first, the net drift was assessed over the full particle trajectory, from shoaling to beaching. The particle trajectories were then analysed per wave zone to examine transitional wave effects in greater detail. Sources of uncertainty were subsequently evaluated, followed by recommendations for future research.

5.1. Particle Drift: Total Travel Distance

It was observed that the mean horizontal drift over the entire distance-shoaling to beaching and thus from $x_p = 0$ until $x_p = 6.5$ metres, decreased as the relative density increased. The relationship between drift speed and relative density is assessed using both a linear and a quadratic fit, which yielded comparable coefficients of determination (R^2). The relatively low R^2 values can be attributed to the wide spread of drift speeds within each category, particularly for particles with lower relative densities. A linear fit was chosen due to the lack of a well-established functional relationship between particle density and transport speed in the literature, and because the category means initially appeared to follow an approximately linear trend. Following the principle of Occam's Razor, which favours the simplest model that sufficiently explains the data, the linear fit was adopted as a first-order approximation.

In addition, an exponential fit was applied to better capture the flattening of the decreasing trend at higher particle densities. Exploring a relationship other than linear is justified by considering fundamental physical principles, which suggest that the interaction between drift and mass is not strictly linear. According to Newton's second law ($F = m \cdot a$), for a given external force F, the acceleration a of a particle is inversely proportional to its mass m. Since drift speed is influenced by the cumulative acceleration over time, this inverse relationship could imply a non-linear dependence between particle mass and drift speed. Moreover, the potentially slightly greater inertia of denser particles further limits their responsiveness to oscillatory wave motion, reinforcing the potentially non-linear nature of the observed trend. Near the end of the spectrum, this exponential fit aligns better with the drift speed value in the 0.93 relative density category.

However, since the R^2 values of both the linear and exponential fits were relatively low, no conclusive mathematical relationship between density and drift speed could be established at that stage. Further research could investigate the underlying causes of the large variability observed within each density category. A better understanding of this variability could result in the development of more accurate and physically meaningful models.

In natural environments, the negative trend in drift speed as density increases means that denser plastic particles are transported more slowly and thus take longer to reach the beach. As a result, particle density directly affects the timing and pattern of plastic debris accumulation on beaches, with denser plastics potentially remaining in the water column longer and depositing later than less dense particles under similar wave conditions. Consequently, it could be speculated that particle density may also influence the spatial pattern of plastic debris accumulation on beaches. For example, particles that remain longer in the water column could be subject to greater lateral displacement by longshore currents, potentially altering their beaching location.

The negative trend found aligned with those of Núñez et al. (2023), who reported that more buoyant particles exhibit higher transport rates, particularly under wave conditions with greater steepness. Their research showed that positively buoyant plastic debris tends to accumulate closer to the shore and is transported more efficiently across the shore, especially when the particles have a larger projected surface area that enhances interaction with surface flows. While Núñez et al. (2023) focused primarily on particle shape and surface area, the current research extends this understanding by isolating the influence of relative density alone, while keeping the size and shape the same. This contributes to the understanding of how density alone influences plastic particle transport, thereby providing a more robust basis for interpreting the separate effects of size, shape and density in future research.

Li et al. (2023) conducted a comparable experiment to the one presented in this research, investigating the transport of 4 cm cubes under wave conditions with an offshore steepness of 0.18 and a beach slope of 1:10. In this research it was observed that particles with a relative density greater than 0.5 were less likely to beach, remaining in periodic motion within the coastal zone and typically staying farther from the slope. In their research, particle trajectories were analysed over a fixed time period of 80 seconds, which meant that not all particles reached the beach. Within this research a fixed spatial domain was applied, tracking particles until they completed their full path through the nearshore zones. Despite this methodological difference, the findings of both studies were broadly consistent: lighter particles reached the beach more easily, whereas heavier particles (RD > 0.5) required more time to do so. Notably, in this research, all particles with RD < 0.5 beached within 80 seconds and all particles with a RD > 0.5 required more than 80 seconds to reach the beach, which aligns with the threshold value at which particles beached described by Li et al. (2023). However, due to the differences in experimental setups direct quantitative comparison between the two studies remains limited. By tracking complete particle trajectories up until particle beaching, this research contributes to understanding breaking and surf zone dynamics by quantifying the reduced drift of high-relative-density particles within these zones.

The estimated drift speeds for all relative density categories fall between the calculated Stokes drift and the phase/ crest speed, but consistently aligning much more closely with the Stokes drift. This suggests that the mean drift speed over the full travel distance (from shoaling to beaching) is best approximated by the Stokes drift for particles with higher relative densities, while for lower-density particles, it corresponds to a value higher than the Stokes drift but below the crest speed.

5.2. Particle Drift: Shoaling Zone

Looking more specifically at the shoaling zone, the zone between the particle release location marked as $x_p = 0$ metres and the beginning of the breaking zone marked with $x_p = 1$ metre, it was observed that within this zone particles generally have a drift speed similar to the estimated local Stokes drift. Particles with a lower relative density tend to have a mean drift speed that is slightly higher than the estimated Stokes drift, whereas particles with a higher relative density tend to have mean drift values slightly lower than the Stokes drift.

A closer look at the lighter RD categories (0.09, 0.15, 0.23, and 0.42 RD) reveals that these categories show a larger spread in drift speeds and have quite a few outliers. This variability suggests a higher level of uncertainty in the drift behaviour of lighter particles within this zone, likely because their low weight makes them easier to move around with little forcing.

This uncertainty makes it harder to determine whether the slightly higher mean and median drift speeds observed for the lighter particles are genuinely above the estimated Stokes drift or simply a result of variability. The poor performance of both the linear and exponential models, as indicated by their low coefficients of determination (R^2 values), suggests that the observed variability may be largely due to experimental noise rather than a consistent underlying physical trend.

Based on previous research regarding non-breaking waves, it was to be expected that within the shoaling zone the particle drift speeds are found to be close to the estimated Stokes drift and that there is a lack of effect of density across a large part of the relative density range. A range of laboratory research—(Calvert et al. 2024; Lenain et al. 2019; Eeltink et al. 2023; Alsina et al. 2020; Larsen et al. 2023) and a review by Poulain-Zarcos et al. (2024), consistently conclude that particles under non-breaking wave conditions have drift speeds comparable to the theoretically estimated Stokes drift. More specifically, in research conducted by Calvert et al. (2024) and Alsina et al. (2020) where density was varied, it was concluded that in deep water conditions and intermediate water depth-for non-breaking waves-particle density was not observed to have any significant effect on drift speed for particles with a relative density below 0.92—the highest density tested in these studies. This is in agreement with the findings of this research, zooming in on the shoaling zone and looking at all relative density categories except 0.93 [-]. This consistency is thus observed both in deep water conditions—where waves are still largely linear—and in the shoaling zone—where wave shapes become increasingly non-linear. The lack of a significant influence of particle density in non-breaking waves, deep water or intermediate, indicates that the transport mechanism prior to wave breaking/ for non-breaking waves is largely independent of density. In a real-world environment, this would imply that particle density, provided the particle remains buoyant and looking only at the contributions of wave forcing, is not a significant factor for predictive models of drift speed and does not affect the speed at which plastics float in the oceans.

Unlike the studies mentioned above, this research reveals an interesting deviation in the behaviour of particles within the 0.93 relative density (RD) category in the shoaling zone, where the drift speed is estimated to be lower than the Stokes drift and lower than any other category. This could hint at a minimal/no effect of density up to a certain threshold value above which density does start to affect drift speed. This suggestion is also made in research conducted by Calvert et al. (2024), which suggests the possibility of a significant effect of relative density that becomes important only when objects approach near-neutrally buoyant. Rather than density alone, it is more likely that this potential shift in behaviour may be more accurately attributed to the particle's buoyancy. As particles approach neutral buoyancy, they submerge deeper below the surface, potentially interacting differently with the wave field than more buoyant particles. In a laboratory flume setting, the interaction between wave-induced Stokes drift and an opposing Eulerian return flow plays a critical role in determining the net transport of floating particles. For intermediate to shallow water waves (kh < 3), theory predicts that the total depth-integrated horizontal mass transport should be zero, with the surface-directed Stokes drift balanced by a return current at depth (Alsina et al. 2020). The Eulerian return flow, which together with the Stokes drift constitutes the total Lagrangian mean flow, exhibits a vertical distribution that becomes increasingly dominant with depth (Monismith 2020). In the present study, the return current was preliminarily quantified by integrating the vertical Stokes drift profile and assuming uniform redistribution along the water depth, revealing its contribution at the surface to be around 43% at the toe of the slope and reaching up to 100% of the surface Stokes drift near the shoreline. This suggests that the presence of a return current may counteract the expected forward drift imposed by Stokes drift. This could explain why drift speeds below the estimated Stokes drift were observed for the 0.93 relative density category, as these particles may behave more like true Lagrangian tracers, moving at a speed that reflects the combined effect of Stokes drift and the opposing Eulerian return flow. While the effect is acknowledged in the current analysis, more accurate quantification of this and other flume-specific hydrodynamic processes is necessary to fully assess their impact on measured particle movement. For the lower-density particles, which exhibit drift speeds close to the estimated Stokes drift, it is hypothesized that the influence of the return current—typically expected to reduce net drift—is either less effective on these particles or offset by other forward-driving processes. These may include residual wave-induced transport or other dynamics, that remain unidentified. In short, the presence of a setup driven return current is acknowledged here, nonetheless, more precise estimates of this process is necessary to consider their influence on the measured particle transport and to determine the potential threshold value above which density starts to play a more significant role.

Nonetheless, the deviation of the highest relative density category (0.93 [-]) observed in this research could potentially indicate the presence of such a shift. The hypothesis regarding the existence of such a shift is also mentioned in research done by Poulain-Zarcos et al. (2024), which states that the behaviour of particles with a slightly positive buoyancy is significantly different from particles with a slightly negative buoyancy. However, it is important to note that the sample size for the highest relative density category was small compared to the other categories, which may reduce the reliability of the observed deviation and increase the potential for bias. Therefore, further research focused specifically on the density range of 0.9–1.0 is warranted to better understand these potential shifts in transport behaviours in relation to density and buoyancy. If a threshold value does exist, it could indicate a distinct point at which particles begin to remain suspended in the water column for longer periods, delaying their arrival in the breaking zone. This prolonged suspension could increase the likelihood of lateral transport by longshore currents or even enhance the chance of particles being carried seaward rather than beaching.

5.3. Particle Drift: Breaking Zone

Concerning the breaking zone, research conducted by Lenain et al. (2019), Deike et al. (2017), Larsen et al. (2023), and Eeltink et al. (2023) concluded that the particle drift speed at the wave breaking point is an order of magnitude larger than for particles in other zones. The drift speeds found in the breaking zone across the range of densities considered in this research align with these findings, as they are 0.6-1.1 orders of magnitude larger than the estimated Stokes drift values. Eeltink et al. (2023) focused on deep-water breaking waves and high relative density particles. While a direct comparison should be made with caution, due to the shallow-water breaking conditions and a different setup used in this research, it is noteworthy that at the breaking point very similar peak drift speeds are observed. For particle densities that are comparable between both studies, the relation to the estimated Stokes drift was also strikingly similar, implying similar transport behaviour in breaking waves in deep and shallow water. Future research could use the breaking wave conditions and research particle drift in both sloped shallow water and deep water setups to conclusively confirm this observation.

Within the breaking zone it was observed that the spread in drift speed values was the largest between all relative density categories. This was to be expected, as Li et al. (2023) observed density-related effects more prominently in the breaking zone than in the shoaling zone, and can be attributed to more turbulence and higher energetic conditions. These conditions were expected to introduce greater variability in how particles are moved, depending on their density and buoyancy. It is important to note that due to these high turbulence conditions inertial effects between different categories cannot be entirely ruled out. These effects are particle-property dependent and may influence particle motion in a way not fully captured by buoyancy and wave characteristics alone. However, density is expected to remain the dominant factor influencing horizontal transport, as the inertial correction to horizontal Stokes drift is relatively small (Santamaria et al. 2013). While this effect may become more relevant for larger macroplastics, it is thus assumed that its effects remain minor compared to the dominant influence of buoyancy and wave-induced drift.

It was observed that all particles began to accelerate and reached their peak drift speed at the same location in the flume along the x-direction. It was seen that particles accelerated over a distance of approximately 1 metre, transitioning from their shoaling zone drift speed—which closely aligned with the estimated Stokes drift—to their peak drift speed. This peak speed varied significantly across density categories. The location of the peak drift speed corresponded closely to the onset of wave breaking. Acceleration began as the wave crest started to tip forward, forming a white bore. The peak speed was reached once the wave collapsed and the bore became fully developed and most turbulent.

Lighter particles reached drift speeds more than ten times greater than the Stokes drift, thus showing a tenfold increase compared to their drift speeds in the shoaling zone under the applied wave conditions. The relative density categories 0.09, 0.15, and 0.23 reached peak drift speeds approaching the estimated crest and phase speed, indicating that the particles moved with the wave—or in other words, “surfed” on the waves—for a short duration as they were taken by the breaking waves. This behaviour aligns with the findings of Larsen et al. (2023), who observed that buoyant microplastics were often caught and transported by breaking waves, where highly buoyant particles moved at speeds close to the wave celerity. Larsen et al. (2023) noted that particles did not remain in the wave front indefinitely. After some distance, the particles tended to become submerged and fell behind the breaking wave. In these cases, a high rise velocity reduced the likelihood of permanent submergence, which allowed particles to resurface more quickly and potentially be recaptured by subsequent breakers. This dynamic enhanced their overall forward transport into the surf zone. The particles near the higher end of the relative density spectrum increased in speed only slightly compared to the lower relative density particles and only reached speeds that were a few multiples higher than the Stokes drift or a fraction of the crest and phase speed. This could be attributed to the higher likelihood of denser particles submerging beneath the wave front (Larsen et al. 2023). In this research, it was observed that these particles were more often overtaken by the wave rather than captured by it, resulting in waves washing over them instead of allowing prolonged “surfing.” Consequently, the duration of acceleration imparted by the wave was shorter, limiting their overall forward transport, which was in line with the findings of Li et al. (2023).

The overall decreasing trend in drift speed as particle density increases in the breaking zone can be approximated by regression. While a linear fit helps illustrate this trend, it unrealistically predicts negative drift speeds at higher densities, highlighting its physical limitations. An exponential model provides a more appropriate representation, as it better respects the physical constraint that drift speed should asymptotically approach zero rather than become negative. This suggests that in predictive models for the breaking zone, drift speed decreases rapidly with density at first but levels off for denser (yet still buoyant) particles due to reduced responsiveness to wave-induced forces. These observations suggest that in real-world coastal environments, once buoyant plastic particles enter the breaking zone, their forward acceleration increases significantly, especially for lower-density plastics. As a result, such particles are likely to be transported shoreward more rapidly and deposited higher on the beach profile. While lighter plastics are more prone to rapid beaching, denser buoyant particles may remain in the surf zone longer, potentially increasing their exposure to mixing or alongshore transport before final deposition.

5.4. Particle Drift: Surf Zone

Throughout the surf zone, the difference in particle drift speed across the density range persists initially but becomes less pronounced as particles approach their final beaching positions. It is important to note that, in this zone, a considerable proportion of particles interacted with the glass side walls, which potentially affected their drift speeds. Additionally, wave propagation speeds estimated in this region—based on the SWASH model—were less reliable, as model performance was determined to deteriorate within the surf zone.

Taking these considerations into account, drift speed estimations throughout this zone were estimated to be higher for low-density particles, especially at the beginning of the surf zone. Higher density particles could be seen to travel with lower drift speeds and more often circle back and forth in the x-direction before they reached the final beaching location. This observation was in line with conclusions drawn by Li et al. (2023), which concluded that transport of high-density particles in the post-breaking zone was reduced compared to low-density particles.

5.5. Density as Predictive Parameter

This laboratory study showed a clear distinction between the different density categories under the tested wave condition, demonstrating that particle density is a key factor influencing the horizontal drift speed of plastic particles in the coastal region, particularly within the breaking zone. In real-world coastal environments, this suggests that lighter plastic particles are more likely to reach the beach quickly and settle closer to their point of entry. In contrast, denser particles may remain suspended in the water column for longer, making them more vulnerable to lateral transport by longshore currents. As a result, they may beach farther from their release location or be carried offshore, contributing to wider spatial distribution and longer residence times in coastal waters.

These findings underscore the importance of density as a predictive parameter in modelling plastic transport. The clear separation in drift speeds between low- and high-relative density categories supports the potential use of density thresholds or categories in transport models to improve accuracy. Since plastic debris in the ocean spans a wide range of densities, integrating this parameter into nearshore transport models could significantly enhance their ability to simulate beaching behaviour and stranding locations.

However, to validate and refine these insights, targeted field research is essential. Field studies are needed to confirm whether the same density-driven trends observed in the controlled flume environment hold in complex natural settings, where factors such as wind, tides, and irregular wave patterns play an important role. Combining laboratory findings with real-world observations will strengthen model development and improve coastal plastic pollution mitigation strategies.

5.6. Limitations and Assumptions

To interpret the results discussed in the sections above it is important to consider the assumptions made and understand the sources of uncertainty within this research. This section will first examine the sources of uncertainty inherent to the laboratory setup, followed by a discussion on the challenges of translating the experimental laboratory findings to real-world coastal environments.

First of all, it was assumed that the wave condition generated was in agreement with the expected wave condition. To verify the accuracy and consistency wave gauges were installed within the flume at six different locations. The measurement analysis (see Section 4.2.1) showed strong agreement between the programmed target wave heights and the measured wave heights. Statistical tests and spectral analysis further supported the assumption that wave conditions remained uniform throughout the experimental period, revealing minimal variation in wave height over time. It was thus concluded that the assumptions regarding the correct generation of the target wave condition and the uniformity of said wave condition over time were met.

Moreover, sidewall interactions may have altered particle drift behaviour. This is a common problem for flume experiments, and is why it is recommended to conduct these experiments in large-scale setups to minimise artificial scale effects that distort wave-particle interactions at the boundary conditions. Especially toward the end of the flume at the end of the surf and throughout the run-up zone, lateral movement increased, as is shown in Figure 4.1. These increased interactions with the side walls, particularly when waves reach the surf zone can potentially be linked to observed wave asymmetries. Waves approached the beach no longer perfectly perpendicular to the flume. It is suspected that these asymmetries are due to interaction with the glass sidewalls, slope and due to reflective waves. This wave asymmetry—causing waves to approach the beach at an angle—is expected to have influenced particle transport near the shoreline. These effects were not numerically verified, but these effects are expected to be minimal—especially compared to ocean waves—and are mostly limited to the end of the surf zone, while this research focuses mainly on the shoaling and breaking zones.

The quality of the particle trajectory data is another source of uncertainty. The main limitation of the tracking process was the performance of the YOLOv5 model used for detection. Several factors affected detection reliability, most of which could be mitigated in future experiments. These included the use of neon yellow tape on the flume bottom, which interfered with detecting similarly coloured particles and areas of shade near the edges of the flume, which changed the particle colour appearance (discussed in more detail in appendix G). Moreover, although it was assumed that the tracking algorithm performed consistently across all density categories, it turned out that the reliability varied. Especially for the densest particle category, the tracking performed less effectively due to the particle being submerged below the water surface more, which resulted in a decreased performance by the YOLO model. On the data gathered by YOLO, filtering techniques were applied to remove inaccurate trajectories, resulting in the used dataset. The data is validated through comparison with manually tracked data in Tracker (see Appendix F). While the filtered data proved reliable and suitable for interpolation, enhancing the tracking algorithm could increase the number of usable trajectories and improve the overall robustness of the analysis.

The SWASH model was used to approximate hydrodynamic conditions across the flume to estimate the wave propagation speeds. Model accuracy was evaluated against measurements from six wave gauges, showing good agreement in the pre-breaking region. However, accuracy progressively decreased beyond the breaking point, which makes sense since SWASH is known to have limitations in simulating post-breaking dynamics (Stelling et al. 2009). SWASH outputs were used to determine wave propagation velocities, which are assumed to be reliable in the shoaling, breaking, and early surf zones—the main focus areas of this research—where deviations were assessed to be a maximum of 24%. The reliability decreases toward the end of the surf zone; however, this region lies outside the primary scope of the study.

Researching plastic transport in a laboratory flume is valuable because the controlled setting makes it possible to study the impact of a single variable in isolation. However, lab-based studies face significant limitations in translating particle behaviour to real-world nearshore environments. The presence of a return current and its effect on drift is mentioned in section 5.2. Additionally, Appendix C.3 presents observations of offshore surface drifts, highlighting the need for further research into the vertical structure of the velocity profile. While similar return currents are present in natural coastal environments, they are generally less pronounced and more variable than those observed in flume settings, where constrained geometry and reflective boundaries can amplify their effects.

Laboratory flume experiments inherently face scaling challenges, particularly in replicating the balance between viscous and inertial forces that govern particle response to wave motion. These forces are typically characterised by non-dimensional numbers such as the Reynolds and Stokes numbers. The Reynolds number characterises the ratio of inertial to viscous forces acting on a particle as it moves through water. The Stokes number describes the ratio of particle inertia to the timescale of the fluid motion, indicating how easily a particle can follow changes in the surrounding flow. Since these values depend on the lab setup, they cannot be directly transferred to real-world conditions without proper dynamic scaling. Even though addressing scaling explicitly could have improved the applicability of the findings to real-world conditions, this research did not include detailed scaling considerations. Nevertheless, the controlled experimental setup still provides valuable insights into the effect of particle density on drift under wave forcing.

Lastly, it is important to note that freshwater was used in this study, rather than the saline water naturally found in marine environments. Due to technical reasons, using saline water in this flume was not possible. Therefore, it is expected that the behaviour when using the same particles would differ slightly in saline water due to a slight shift in the density of the water and thus in relative density. However, since the relative densities in this research were calculated based on the density of fresh water, the reported values for relative density remain accurate.

In summary, while several sources of uncertainty were identified, the collective impact is primarily reflected in increased scatter in the trajectory data rather than systematic bias. The filtering and validation steps applied to the trajectory dataset ensured that only reliable data was used in the analysis, and the focus on zones where the model and measurement were most reliable further minimised potential errors. Throughout the results the scatter in the data is always acknowledged using confidence interval whiskers. Therefore, although these uncertainties may have introduced variability, they do not compromise the conclusions described above. The observed trends in particle drift behaviour as a result of variations in density are significant given the data uncertainty.

5.7. Future Research

While this research offers a valuable contribution to understanding plastic particle transport under controlled wave conditions, there remains a wide range of exciting opportunities for further exploration.

First of all, the relationships identified in this research should be tested in real-world nearshore environments. By isolating specific variables under controlled laboratory conditions, this research aims to enhance the understanding of plastic transport in natural coastal settings. However, it is important to acknowledge that actual nearshore environments are significantly more complex than the simplified conditions simulated in the laboratory flume. Field research conducted by Haagsma (2025) in the nearshore region of the North Sea found that heavier drifters took longer to beach compared to lighter ones. Her study suggested that this could be attributed to deeper submersion and a reduction in surfing behaviour, which aligns with the findings of the current research. Additional field studies could further strengthen this conclusion.

This research, along with research conducted by Calvert et al. (2024) and Poulain-Zarcos et al. (2024), proposes a potential shift in the influence of particle density and buoyancy as particles approach neutral buoyancy. Within this research a density range between 0.09-0.93 [-] was investigated, but future research could focus on particles in the range of 0.90-1.0 relative density. Investigating the transport dynamics of particles with near-neutral buoyancy could significantly enhance our understanding of how subtle density variations influence drift and transport behaviour in wave-dominated environments.

Similar experiments could be conducted using irregular waves based on a realistic wave spectrum. An indication of the validity of the approach used in this research is provided by Núñez et al. (2023), who investigated the effects of both regular and irregular waves on plastic transport. Their research found that the transport behaviour under the irregular wave condition—characterised by a target wave signal falling between those of two regular wave conditions—yielded results falling in the middle of the range-as expected. This suggests that regular waves can serve as a reasonable representation of overall transport trends. However, they also noted that transport processes are influenced by the differing time scales inherent to regular versus irregular wave conditions, highlighting the importance of considering these temporal dynamics in future research.

Research by Cocozza (2025) examined the influence of wave steepness on particle transport in the nearshore zone, a topic also explored in the study by Li et al. (2023). However, in both studies the particle density was kept constant as wave steepness changed. This research varies density, but only investigates one wave condition and thus one wave steepness profile. An expansion on the current research, which can be executed using the same setup, would be to vary the density for multiple wave-steepness values. This would enable deeper investigation into the complex relationship between wave characteristics and particle properties.

While this research explored the relationship between drift speed and relative density across both the total transport distance and specifically within the breaking zone, the findings did not yield a single conclusive trend—linear and exponential relationships both showed relatively strong fits with comparable R^2 values. Further investigation into the precise nature of this relationship is recommended, as a clearer understanding would significantly enhance future modelling efforts of plastic particle transport.

Another relevant consideration is the size of the particles considered in this research. All particles were identical in shape and size—spheres with a diameter of 4 centimetres. When compared to the offshore wavelength determined in this research, the particles represent approximately 1.4 % of the wavelength. However, as the water depth decreases along the slope, the wavelength shortens, and near the end of the surf zone, the relative particle size increases to about 5 % of the local wavelength. Xiao et al. (2025), Poulain-Zarcos et al. (2024), and Calvert et al. (2024) state that drift enhancement resulting from size for very small objects is limited. Particle size appears to have no influence on the drift of buoyant particles as long as the particle size compared to the wavelength does not exceed 1.5% (Poulain-Zarcos et al. 2024), while larger particles can experience significant drift enhancement due to their relative size, often travelling faster than the predicted Stokes drift. In this research, the wave condition remained constant, and all particles were of the same size across the different categories tested, meaning that size-related drift enhancement is not an additional variable between different density categories. Nonetheless, the influence of particle size on wave propagation speeds—and how this effect changes with varying wavelength along the slope—warrants further investigation.

Future research should also explore the role of biofouling—a process in which microorganisms and other marine life attach to floating plastic particles—as it is suggested to have a significant effect on plastic transport. As biofilms develop on the surface of plastics, the overall mass changes, which affect the particle's density and buoyancy, potentially leading to a gradual shift in relative density that may result in sinking. This phenomenon has been documented in several recent studies. Understanding how biofouling alters particle density over time is essential and can be directly related to the results found in this research.

Legend: ▬ 100% overlap ▬ 90% overlap with minimal adjustments ▬ 0% overlap

6

Conclusion

In this research, the influence of particle density on the nearshore transport of marine plastic debris was studied. This was accomplished by conducting laboratory experiments across a sloped bathymetry, using controlled regular waves. The results demonstrate that the horizontal drift and beaching dynamics of marine plastic debris are dependent on particle density, with the strongest dependence observed in the breaking zone. A clear negative relationship is observed between density and drift speed, as higher-density particles take significantly longer to reach the beach compared to lower-density particles.

In the shoaling zone, drift speed is largely independent of particle density and closely matches theoretical estimates of local Stokes drift, up to relative densities approaching neutral buoyancy. As the relative density approaches neutral buoyancy, a possible shift in density dependence is observed, though further investigation is needed. All particles, regardless of density, begin to accelerate at a consistent location within the flume—coinciding with the first overtopping of waves—marking the start of the breaking zone. From this point onward, drift behaviour becomes density-dependent. Low-density particles accelerate more strongly, often reaching drift speeds comparable to local phase and crest speeds, while high-density particles show only limited acceleration. Thus, a strong negative relationship is observed, with higher-density particles travelling significantly slower. To better capture the decreasing drift speed at the higher end of the density range, an exponential relationship is explored, though the exact nature of the relationship requires further investigation. In the surf zone, the initial variability in drift speeds across densities gradually decreases.

This study focuses on particle density under a single wave condition, while Cocozza (2025) simultaneously examines the influence of wave steepness for a single density, and thus approaches the problem from a wave dynamics perspective. The study found a clear positive relationship between offshore wave steepness and the horizontal drift speed of marine plastic debris, with steeper waves consistently leading to faster transport. Together, these two studies highlight that both wave properties and particle characteristics play an important and interrelated role in determining transport behaviour.

To further build on the results yielded in the current study, field validation is crucial. Real-world studies are needed to test whether the observed trends persist under natural conditions, where additional forces like wind, tides, and variable wave patterns influence transport. Parallel to this study, research by Haagsma (2025) conducted on the beach near Scheveningen found that heavier drifters took longer to beach compared to lighter ones, consistent with the findings of the present study. However, Haagsma (2025) also concluded that the complexities of real coastal dynamics introduce additional factors influencing plastic transport not accounted for in this study, such as wind and its direction, cross-shore currents, and tidal influences. Continuing to bridge lab and field insights will support more effective modelling and inform better strategies to manage coastal plastic pollution.

This study shows that for the non-breaking wave condition tested, particle drift is largely independent of density. Based on this research in shallow water and supported by literature, this trend appears consistent across shallow, intermediate, and deep water conditions. However, once wave breaking occurs—a key process in the nearshore zone—density becomes a major factor influencing transport behaviour. Given the wide range of plastic densities in the ocean, this found dependency highlights density as a key factor in predicting plastic transport in the near-shore region. The clear differences in drift speeds between low- and high-density particles suggest that considering density as an parameter could improve transport and beaching models.

Bibliography

Alsina, José M et al. (2020). “Laboratory measurements of the wave-induced motion of plastic particles: Influence of wave period, plastic size and plastic density”. In: *Journal of Geophysical Research: Oceans* 125.12, e2020JC016294.

Antrim, Jim (1981). *Wave Action - How and Why Waves Behave As They Do*. `https://www.antrimdesign.com/waves`. Accessed: 2025-06-02.

Booij, Nico (1981). “Gravity waves on water with non-uniform depth and current”. In: *Ph. D. Thesis*.

Calvert, R et al. (2024). “A laboratory study of the effects of size, density, and shape on the wave-induced transport of floating marine litter”. In: *Journal of Geophysical Research: Oceans* 129.7, e2023JC020661.

Cocozza, C. (2025). “Influence of Wave Steepness on the Beaching of Marine Plastic Debris: Insights from Laboratory Flume Experiments”. Master’s thesis in preparation.

Cózar, Andrés et al. (2014). “Plastic debris in the open ocean”. In: *Proceedings of the National Academy of Sciences* 111.28, pp. 10239–10244.

Critchell, Kay et al. (2015). “Modelling the fate of marine debris along a complex shoreline: Lessons from the Great Barrier Reef”. In: *Estuarine, Coastal and Shelf Science* 167, pp. 414–426.

Deike, Luc et al. (2017). “Lagrangian transport by breaking surface waves”. In: *Journal of Fluid Mechanics* 829, pp. 364–391.

Eeltink, Debbie et al. (2023). “Stochastic particle transport by deep-water irregular breaking waves”. In: *Journal of Fluid Mechanics* 971, A38.

Eriksen, Marcus et al. (2014). “Plastic pollution in the world’s oceans: more than 5 trillion plastic pieces weighing over 250,000 tons afloat at sea”. In: *PloS one* 9.12, e111913.

Fenton, John D. (1988). “The numerical solution of steady water wave problems”. In: *Computers & Geosciences* 14.3, pp. 357–368.

Haagsma, I. (2025). “Investigating the beaching dynamics of plastic in the nearshore region: a Fieldwork study”. Master’s thesis in preparation.

Hedges, Terry S (1976). “An empirical modification to linear wave theory.” In: *Proceedings of the Institution of Civil Engineers* 61.3, pp. 575–579.

Holthuijsen, Leo H. (2007). *Waves in Oceanic and Coastal Waters*. Cambridge, UNITED KINGDOM: Cambridge University Press. ISBN: 978-0-511-26845-8. (Visited on 01/02/2025).

Jambeck, Jenna R et al. (2015). “Plastic waste inputs from land into the ocean”. In: *science* 347.6223, pp. 768–771.

Kaandorp, Mikael LA et al. (2020). “Closing the Mediterranean marine floating plastic mass budget: inverse modeling of sources and sinks”. In: *Environmental science & technology* 54.19, pp. 11980–11989.

Larsen, Bjarke Eltard et al. (2023). “Experimental investigation on the nearshore transport of buoyant microplastic particles”. In: *Marine Pollution Bulletin* 187, p. 114610.

Lenain, Luc et al. (2019). “Laboratory studies of Lagrangian transport by breaking surface waves”. In: *Journal of Fluid Mechanics* 876, R1.

Li, Huichao et al. (2023). “Beaching process of floating marine debris associated with the evolution of the nearshore wave”. In: *Marine Pollution Bulletin* 197, p. 115695.

Löhr, Ansje et al. (2017). “Solutions for global marine litter pollution”. In: *Current opinion in environmental sustainability* 28, pp. 90–99.

Martins, Kévin et al. (2021). “Dispersive characteristics of non-linear waves propagating and breaking over a mildly sloping laboratory beach”. In: *Coastal Engineering* 168, p. 103925.

McClenaghan, Elliot (2024). *Mann-Whitney U Test: Assumptions and Example*. `https://www.technologynetworks.com/informatics/articles/mann-whitney-u-test-assumptions-and-example-363425`. Accessed: 2025-05-07.

Melanie (Mar. 28, 2024). *You Only Look Once (YOLO): What is it?* Accessed: 2025-05-07. DataScientest. URL: `https://datascientest.com/en/you-only-look-once-yolo-what-is-it`.

Monismith, Stephen G (2020). “Stokes drift: theory and experiments”. In: *Journal of Fluid Mechanics* 884, F1.

Myrhaug, Dag et al. (1986). “Steepness and asymmetry of extreme waves and the highest waves in deep water”. In: *Ocean Engineering* 13.6, pp. 549–568. DOI: `10.1016/0029-8018(86)90039-9`.

Núñez, Paula et al. (2023). “Wave-induced cross-shore distribution of different densities, shapes, and sizes of plastic debris in coastal environments: A laboratory experiment”. In: *Marine Pollution Bulletin* 187, p. 114561.

Onink, Victor et al. (2021). “Global simulations of marine plastic transport show plastic trapping in coastal zones”. In: *Environmental Research Letters* 16.6, p. 064053.

Plus, Machine Learning (2023). *Augmented Dickey-Fuller Test in Python: Complete Guide*. Accessed: 2025-05-18. URL: `https://www.machinelearningplus.com/time-series/augmented-dickey-fuller-test/`.

Poulain-Zarcos, Marie et al. (2024). “Laboratory experiments related to marine plastic pollution: a review of past work and future directions”. In: *Comptes Rendus. Physique* 25.S3, pp. 1–32.

Santamaria, Francesco et al. (2013). “Stokes drift for inertial particles transported by water waves”. In: *Europhysics Letters* 102.1, p. 14003.

Soulsby, Richard (1997). “Dynamics of marine sands”. In.

StatsKingdom (2024). *Shapiro-Wilk test with tables*. Accessed: 2025-05-01. URL: `https://www.statskingdom.com/doc_shapiro_wilk.html`.

Stelling, GS et al. (2009). “Numerical modeling of wave propagation, breaking and run-up on a beach”. In: *Advanced computational methods in science and engineering*. Springer, pp. 373–401.

Team, SWASH Development (2025). *SWASH User Manual*. Accessed May 5, 2025. URL: `https://swash.sourceforge.io/online_doc/swashuse/swashuse.html%5C#file-swashedt`.

Tissier, M. et al. (2011). “Field measurements and non-linear prediction of wave celerity in the surf zone”. In: *Coastal Engineering* 58.7, pp. 701–712. DOI: `10.1016/j.coastaleng.2011.03.003`.

TU Delft Faculty of Civil Engineering and Geosciences (n.d.). *Indoor Lab Facilities – Hydraulic Engineering Laboratory*. `https://www.tudelft.nl/citg/over-faculteit/afdelingen/hydraulic-engineering/sections/hydraulic-engineering-laboratory/indoor-lab-facilities`. Accessed: 2025-04-13.

Van den Bremer, Ton S et al. (2017). “Stokes drift”. In: *Philosophical transactions of the royal society a: mathematical, physical and engineering sciences* 376.2111, p. 20170104.

Van der Zanden, Joep (2016). “Sand transport processes in the surf and swash zones”. In.

Van Sebille, Erik, Stefano Aliani, et al. (2020). “The physical oceanography of the transport of floating marine debris”. In: *Environmental Research Letters* 15.2, p. 023003.

Van Sebille, Erik, Chris Wilcox, et al. (2015). “A global inventory of small floating plastic debris”. In: *Environmental Research Letters* 10.12, p. 124006.

Wikipedia contributors (2024). *Kruskal–Wallis test — Wikipedia, The Free Encyclopedia*. Accessed: 2025-05-07. URL: `https://en.wikipedia.org/wiki/Kruskal%E2%80%93Wallis_test`.

– (2025). *Bonferroni correction — Wikipedia, The Free Encyclopedia*. `https://en.wikipedia.org/wiki/Bonferroni_correction`. Accessed: 2025-06-02.

Xiao, Q et al. (2025). “Laboratory study of the enhanced wave-induced drift of large rectangular floating objects”. In: *Journal of Fluid Mechanics* 1008, A18.

A

Camera Calibration Distance Conversion

To translate the observed movement of particles in the video recordings into real-world trajectories within the flume, camera calibration was required. The camera calibration procedure considered in this study consisted of two components: The correction of lens-induced image distortion, and relating camera pixel-distances to real-world distances.

A.1. Camera Distortion

Camera distortion is the geometric warping of images caused by the camera lens, resulting in curved lines or altered shapes, especially at the edges of wide-angle images. In the original recordings used in this research, distortion appeared minimal. The bottom of the flume —representing a real-world straight line across the entire frame— remained visually straight in the recordings as long as the GoPros were set to linear mode. Nevertheless, to quantitatively assess and confirm the extent of distortion, undistortion methods were applied. A Python script, shown in full in Appendix H, using OpenCV was used to correct for lens distortion. The calibration process began by shooting a calibration video in which the camera was set in place and a 9×7 checkerboard with 75 mm squares was moved throughout the camera window in different locations and under varying angles. Frames were extracted from the calibration video, and the code mapped the 2D image coordinates of the squares on the board. This resulted in a set of object points (real-world coordinates) and image points (corresponding image coordinates), which were then used to estimate the specific camera parameters. The results of this were a camera matrix and distortion coefficients. These were applied to the videos, resulting in undistorted footage. The working calibration procedure was applied to multiple representative video recordings for the footage used in this research. A comparison between the original and the undistorted videos confirmed that the magnitude of the distortion in these videos was on the order of millimetres, even at the edges of the camera's field of view where distortion was expected to be the most significant. Given that the observed distortion was limited and considering that the particle travel distances in this study are on the order of metres, such a minor offset was deemed negligible. The videos used in this research were therefore not corrected for distortion.

A.2. Distance Conversion

To establish an accurate relationship between recorded pixel-distances and real-world distances, spatial reference markers were introduced into the experimental setup. Reference markers with known real-world distances were placed on the interior glass walls of the flume in both the direction of the flume's length (x) and width (y) for the top-view cameras as can be seen in Figure A.1A. For the side-view cameras, the markings were made on the outside of the glass to mark once again in the direction of the length of the flume (x) and the height of the flume (z) as shown in Figure A.1B. These markers were clearly visible in the video footage and served as fixed reference points, enabling the derivation of a pixel-to-real-world distance ratio. This approach allowed for consistent and accurate conversion of tracked particle positions from pixel coordinates to metric units across all recordings.

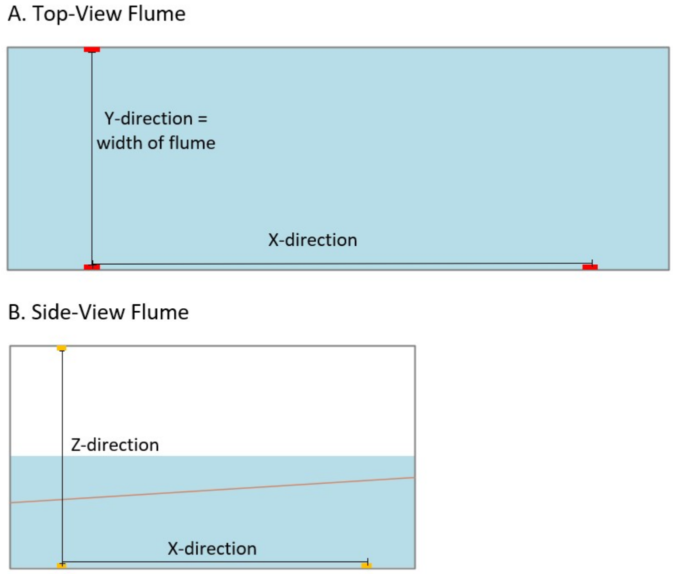

Figure A.1: Schematic showing the use of reference frames in the flume

Legend: ▬ 100% overlap ▬ 90% overlap with minimal adjustments ▬ 0% overlap

B

Particle Design Process

As described in Section 3.2.3, a set of particles representing different weight categories was used. For each weight category, two identical particles were fabricated, with the exception of the highest weight category, which contained only a single particle. Table B.1 shows in short how each of the particles for each category was made. Several Particles were borrowed from research conducted by, among others, T. van den Bremer described in the article ”A Laboratory Study of the Effects of Size, Density, and Shape on the Wave-Induced Transport of Floating Marine Litter” (Calvert et al. 2024) and were only repainted for this research. The lightest particles were painted ping pong balls. The other particles were made by increasing the weight of store-bought ping pong balls, for which the exact process is described below.

Category	Approximate Weight [g]	Relative Density [-]	Design
1	3.0	0.09	Empty Ping Pong ball
2	5.1	0.15	Borrowed from T. van den Bremer
3	7.7	0.23	Self Made
4	13.8	0.41	Self Made
5	23.1	0.69	Borrowed from T. van den Bremer
6	25.2	0.75	Borrowed from T. van den Bremer
7	31.3	0.93	Self Made

Table B.1: Table of Category, Approximate Weight, Relative Density, and Design

Particles Barrowed from T. van den Bremer:

The particles used in this research were originally developed for a similar flume study. The 5-gram particles consisted of hollow plastic spheres, while the heavier particles (23 [g] and 25 [g]) were identical plastic spheres filled with a resin material to increase their mass.

During the experiments, it was observed that the heaviest particles consistently oriented themselves in the same way when submerged in water, with the same side always facing upward. This behaviour suggests an uneven internal distribution of mass, likely due to an inhomogeneous filling process. Such an imbalance may influence the particles’ rotational dynamics, potentially affecting their spinning and turning behaviour during the experiments.

Self Made Particles:

Before the actual design, a target weight was determined to create a step-by-step increase in Relative Density [-] for the particles. The target weights for the categories were 7.5 grams, 13 grams and 32 grams. The particles were made in the following way:

1. Each ping pong ball was carefully cut in half, and a thin layer of glue was applied to the inside

of the two halves.

2. A weighted amount of sand or fine gravel was evenly distributed across the glued side surfaces to achieve a uniform mass distribution.
3. After allowing the glue to dry completely, the weight of the two halves was checked. If the total mass did not meet the target value, additional material was added accordingly.
4. The hollow interiors of the two halves were filled with polyurethane (PU) foam, and the halves were reassembled and pressed together to form a sealed sphere.
5. Before the foam fully hardened, the alignment of the two halves was carefully adjusted to ensure proper shape and symmetry. If needed, superglue was applied to secure the final positioning.
6. Once the assembled spheres were fully dried, their outer surfaces were roughened using sandpaper to enhance paint adhesion. Each particle was then individually spray-painted in a specific colour for identification during tracking.

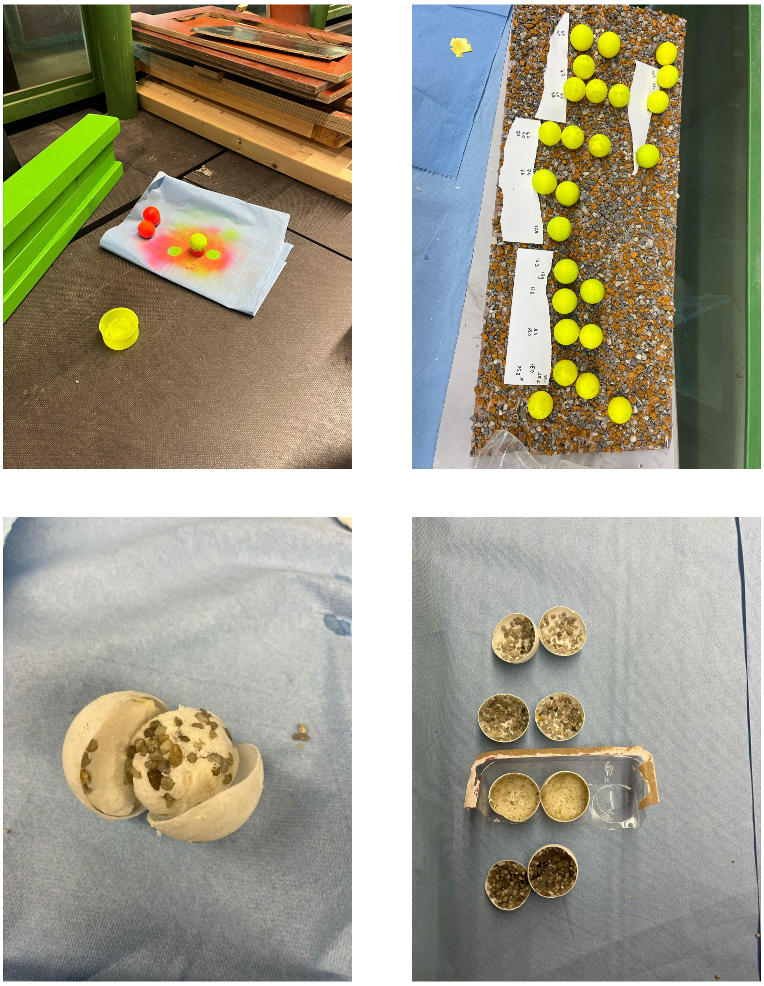

Figure B.1: Images of the process of fabricating the self-made particles.

C

Initial Testing and Setup Refinement

To gain a better understanding of the hydraulic dynamics within the flume and to establish a robust experimental procedure, the setup underwent a series of preliminary tests and adjustments.

C.1. Spin-up Time

Prior to the experimental campaign, the spin-up time was estimated. The spin-up time refers to the time needed for the initial turbulence caused by wave generation to decay in the flume. Once the wave maker was turned on, the paddle started moving forwards and backwards, pushing against the body of water. This initial motion introduced a turbulence in the form of eddies and vortices near the paddle. A stabilization period is required to allow these disturbances to propagate downstream towards the end of the flume, enabling the system to reach quasi-steady state along the length of the flume.

The time required to reach this steady state, the spin-up time, was estimated to be five minutes for the experimental setup used in this research. No experiments were conducted within these initial five minutes.

This estimation was based on observations using floating particles. A measurement window was established along the flume with a fixed horizontal distance x. Immediately after activating the wave generator, particles were released, and their travel time across this distance was measured over approximately 15 minutes. These measurements were conducted for wave conditions with a period of 1.5 seconds and wave heights of 0.05 metres and 0.20 metres. It was observed that the particles travel speed was highest during the first minutes, and after approximately four to five minutes, the travel speed stabilized. It was therefore decided to wait 5 minutes after starting the wave maker before beginning the experiment.

C.2. Instrument Deployment Strategy

As outlined in Section 3.1.3, six wave gauges sensors were placed along the flume length during this study. Prior to conducting the experiments, the target wave condition was measured by running it for 25 minutes: a 5-minute spin-up period to stabilize the wave field, followed by 20 minutes of measurements. This procedure generated wave data at six distinct locations along the flume for each wave condition. Following these measurements, wave gauges 2–6 were removed to prevent potential interference between the sensors and plastic particles during subsequent particle-tracking experiments. The assumption was made that the wave gauge data collected prior to particle deployment would remain representative of the wave conditions during the particle experiments, as the experimental set up and settings of the wave maker remained the same during those experiments. To validate this assumption and collect additional wave condition data, the wave gauge sensor placed in Location 1 was kept in place during the particle experiments, as it was positioned behind the particle deployment location, avoiding any risk of sensor-particle interaction.

C.3. Tipping point

During initial trial runs, it was observed that, following the spin-up period, floating particles introduced behind the shoaling zone experience a negative drift towards the wave generator. Specifically, particles placed further offshore (closer to the wave maker) in the flume consistently drifted towards the wave maker rather than in the onshore direction. This indicates the presence of a surface drift directed away from the beach. However, particles placed right before the breaking point of the wave all travelled towards the beach. It was thus observed that a tipping point appears to exist at which particles either drift onshore or offshore. To test the dynamics, various wave conditions (ranging wave heights) were tested. The location of this tipping point—or tipping zone—relative to the breakpoint shifted further offshore as the wave height increased under constant wave period conditions.

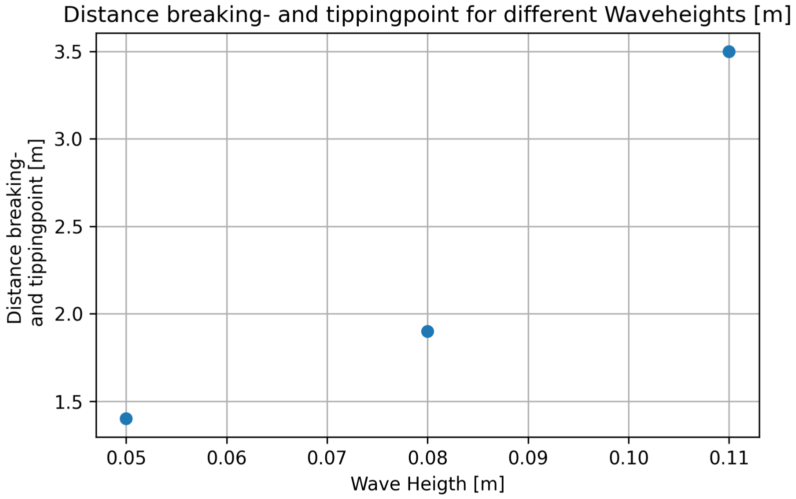

Figure C.1: The distance between the breaking and tipping point in metres expressed as a function of wave heights in the experimental setup.

To give an indication, C.1 shows the distance between the breaking point and the estimated tipping point-or tipping zone- for several wave height. In the figure it can be seen that as the wave height increases, the tipping point moves further backward when compared to the breaking point. For wave heights of 0.17 metres or greater, all particles along the entire length of the flume appeared to travel towards the beach, with no negative surface drift observed at any location.

To better understand the dynamics in the flume, sinking particles were released. The sinking particles placed at the toe of the slope were observed to be moving forwards towards the beach at increasing speed as they approached the breaking point. The particles were observed to collect at the breaking point, where they remained stationary. Sinking particles initially placed on the beach, downstream of the breaking point, travelled backwards towards the breaking zone until they also settled in that region. All sinking particles ultimately collected at the bottom of the flume at the wave breaking point.

C.2 describes the observations made for the wave heights 0.05, 0.08 and 0.11 metre. As the wave height was increased, the breaking zone and tipping zone moved offshore in the flume towards the wave generator, the general directions are described in Figure C.2. As previously mentioned, all sinking particles observed to accumulate at the wave breaking point, referred to as the collection zone in the figure. Particles released beyond the tipping point tended to settle at the end of the slope, referred to here as the ‘beach’. It is expected that particles transported in the backward direction would accumulate near the wave maker, at the upstream end of the flume. However, the exact location of this potential collection zone could not be confirmed, as particles were retrieved approximately three metres before reaching the wave maker for safety reasons.

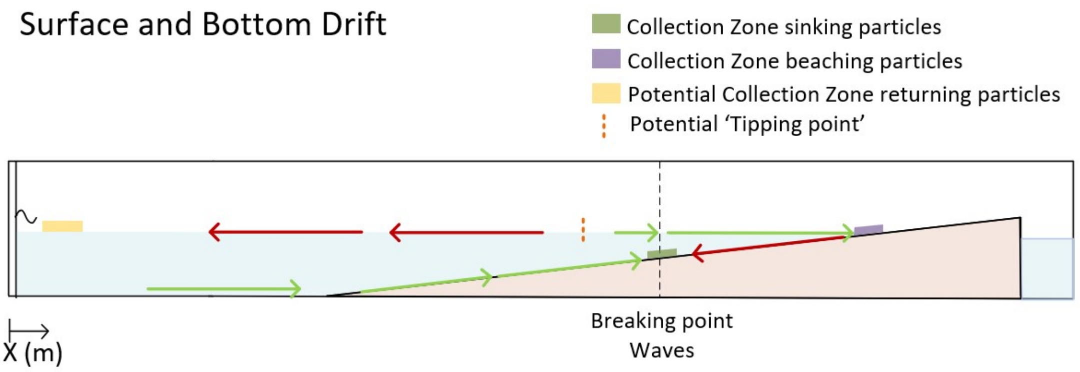

Figure C.2: Schematic of the drift directions observed for wave height 0.05 m, 0.08 and 0.11 m

Based on these observations, and considering the limitations imposed by the maximum length of the observation window, it was decided to release the floating plastic particles within the shoaling zone, 1.5 metres upstream of the the wave breaking point. This placement consistently resulted in all particles reaching the beach. However, further research should be conducted investigating the vertical structure of the velocity profile. Understanding how surface and near-bed flows interact across different wave conditions could provide deeper insight into the mechanisms governing particle transport and accumulation within the flume, and would allow for a better understanding of how it relates to reality. However, this was beyond the scope of this research and is thus not further investigated in this report.

Legend: ▬ 100% overlap ▬ 90% overlap with minimal adjustments ▬ 0% overlap

D

SWASH Model

In the context of this study, a SWASH model was used to simulate the experimental wave conditions within the flume. This was done in order to fully understand the wave dynamics in the longitudinal direction for the investigated wave condition. In this appendix the input file provided to the model is described to allow reproducibility of the methodology presented in 3.5.

D.1. Model Input

The user should provide SWASH with a number of files with the following information:

- A file containing the instructions of the user to SWASH (the command file);
- File(s) containing: grid, bottom, (initial) current and water level;
- File(s) containing boundary conditions.

The mentioned files are made available in a GitHub repository accessible from Appendix H.

D.1.1. Command File

The command file is a plain text input file which contains all the necessary instructions to define:

- Simulation type
- Domain geometry
- Physical settings
- Boundary conditions
- Output options

An example of input file (H11.sws) is provided below in Figure D.1. This specific input file was created to simulate regular waves with a wave height of 0.11 metre and a wave period of 1.5 seconds propagating over a sloped bottom of 1:40.

A brief description of the input commands is provided below, more information can be found in the software manual available at (Team 2025).

1. Definition of computational grid: the model is defined in 1D mode with normally incident waves propagating over a uniform beach. The simulation extent origin is set at x = 0 and reaches up to x = 35 metre with 350 computational cells. In the vertical direction, a three layers discretization is applied.
2. Definition of bottom profile: the bathymetry of the flume is provided to the model by the file ”bed_profile.bot”.

3. Physics: some physical features are specified. The mode is set to non-hydrostatic, the breaking model is activated and a standard friction coefficient is specified.
4. Boudary conditions: the still water level is specified and set to 0.5 metre. The boundary condition definition line specifies the location of the boundary to be on the West side (W) of the domain with a counter-clockwise direction (CCW). Continuous regular waves are programmed (CON REG) representing the monochromatic wave input with a wave height of 0.109 metres (in accordance with the mean wave height computed from the experimental data) and a period of 1.5 seconds.
5. Output request(s): six measuring locations are defined following the real experimental setup.
    - The ”POINT” command defines a point output with specified name and location in the longitudinal direction. The variables time in seconds (TSEC), surface elevation (WATLEV) and velocity (VEL) are requested as output for every point and stored every 0.05 seconds (Fs = 20 Hz) in a ”.tbl” file. This pattern is repeated for gauges 1 to 6 at different positions following the experimental setup described in Section 3.1.3.
    - The ”GROUP” command defines a group of points over a subgrid from cell 1 to 350 in x-direction. The variables time in seconds (TSEC), x-position (XP), surface elevation (WATLEV), bed elevation (BOTLEV), velocity (VEL) and water depth (DEPTH) are simulated every 0.05 seconds (Fs = 20 Hz). This output provides the continuous wave dynamics over the longitudinal direction.

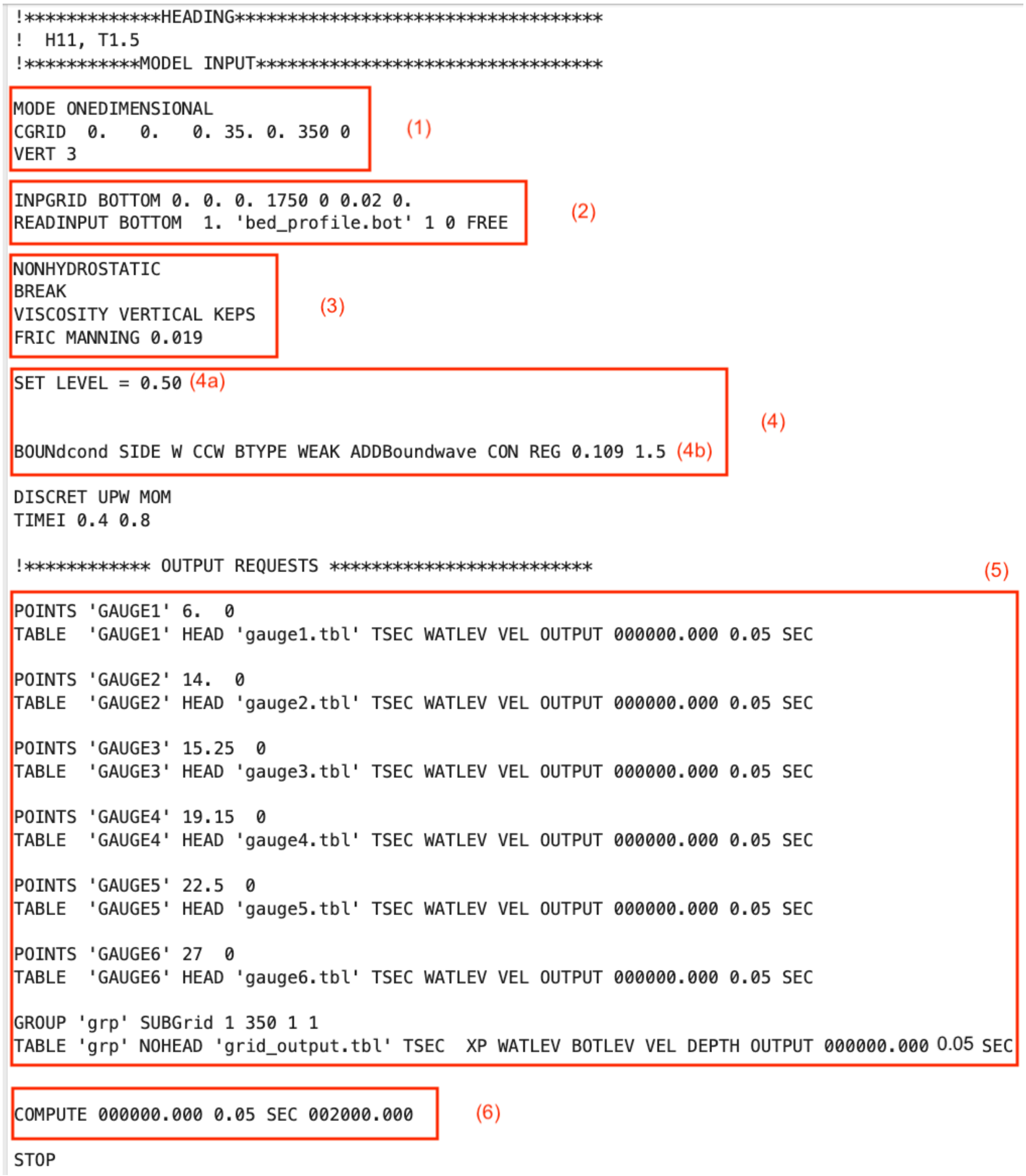

```
!*************HEADING***********************************
!  H11, T1.5
!***********MODEL INPUT*********************************
MODE ONEDIMENSIONAL
CGRID  0.   0.   0. 35. 0. 350 0
VERT 3
INPGRID BOTTOM 0. 0. 0. 1750 0 0.02 0.
READINPUT BOTTOM  1. 'bed_profile.bot' 1 0 FREE
NONHYDROSTATIC
BREAK
VISCOSITY VERTICAL KEPS
FRIC MANNING 0.019
SET LEVEL = 0.50


BOUNdcond SIDE W CCW BTYPE WEAK ADDBoundwave CON REG 0.109 1.5

DISCRET UPW MOM
TIMEI 0.4 0.8

!************ OUTPUT REQUESTS *************************

POINTS 'GAUGE1' 6.  0
TABLE  'GAUGE1' HEAD 'gauge1.tbl' TSEC WATLEV VEL OUTPUT 000000.000 0.05 SEC

POINTS 'GAUGE2' 14.  0
TABLE  'GAUGE2' HEAD 'gauge2.tbl' TSEC WATLEV VEL OUTPUT 000000.000 0.05 SEC

POINTS 'GAUGE3' 15.25  0
TABLE  'GAUGE3' HEAD 'gauge3.tbl' TSEC WATLEV VEL OUTPUT 000000.000 0.05 SEC

POINTS 'GAUGE4' 19.15  0
TABLE  'GAUGE4' HEAD 'gauge4.tbl' TSEC WATLEV VEL OUTPUT 000000.000 0.05 SEC

POINTS 'GAUGE5' 22.5  0
TABLE  'GAUGE5' HEAD 'gauge5.tbl' TSEC WATLEV VEL OUTPUT 000000.000 0.05 SEC

POINTS 'GAUGE6' 27  0
TABLE  'GAUGE6' HEAD 'gauge6.tbl' TSEC WATLEV VEL OUTPUT 000000.000 0.05 SEC

GROUP 'grp' SUBGrid 1 350 1 1
TABLE 'grp' NOHEAD 'grid_output.tbl' TSEC  XP WATLEV BOTLEV VEL DEPTH OUTPUT 000000.000 0.05 SEC

COMPUTE 000000.000 0.05 SEC 002000.000

STOP
```

Figure D.1: Example of SWASH input file.

Legend: ▬ 100% overlap ▬ 90% overlap with minimal adjustments ▬ 0% overlap

E

Preliminary Particle Drift Analysis

The transport behaviour of plastic particles within the flume was analysed based on multiple spatial scales. This section explores how this was done by first examining the computation of total travel velocities. The flume was then divided into hydrodynamic zones (shoaling, breaking, surf, and swash) and particle velocities were measured in each zone to better understand the plastic transport.

E.0.1. Total Travel Velocity

During the experimental campaign, the total travel time of each particle was manually recorded using a stopwatch, as outlined in Section 3.3. The moment of release in the shoaling zone and the moment of beaching—defined as the point at which the particle came to rest on the slope—were noted for each particle. A total of approximately 70-100 particles were measured for each category, except for the last category (density=0.93), for which only 25 particles were used. The total travel distance covers the full extent of the nearshore zone—including the shoaling, breaking, surf, and swash zones—and ranges from 6.5 to 7.3 metres. This variation arises from differences in beaching locations among the density categories, with lighter particles tending to travel farther up the beach. The travel time combined with the measured total travel distance enables a first estimation of particle travel speed across the various categories for relative particle density.

All manually recorded observations were transcribed and organised into their respective categories. For each category, mean travel speeds were calculated based on 25 to 100 observations. The data was used to calculate the mean travel speed for each category displayed in Figure E.1, as well as assessing the variability within categories.

First, it was assessed whether the travel speed data follows a normal distribution using the Shapiro-Wilk test, applying a significance level of 0.05 (StatsKingdom 2024).

Once the nature of the distribution was assessed to be not normally distributed, initially a Kruskal–Wallis test was conducted (Wikipedia contributors 2024). This test is suitable for comparing more than two independent groups when the assumption of normality is not met. This initial statistical test was used to identify whether any of the categories showed significant differences in travel speed, which can indicate the need for a more detailed pairwise comparison in the following analysis.

When the Kruskal–Wallis test indicated that at least one group differs significantly in median, a more detailed pairwise analysis was required to determine which specific groups show statistically significant differences. This was done using the Mann–Whitney U test, a non-parametric test used to assess whether two independent samples originate from the same distribution (McClenaghan 2024). It was assumed that all observations are independent. The null hypothesis (H_0) assumes that both groups have the same distribution, while the alternative hypothesis (H_1) assumes that the distribu-

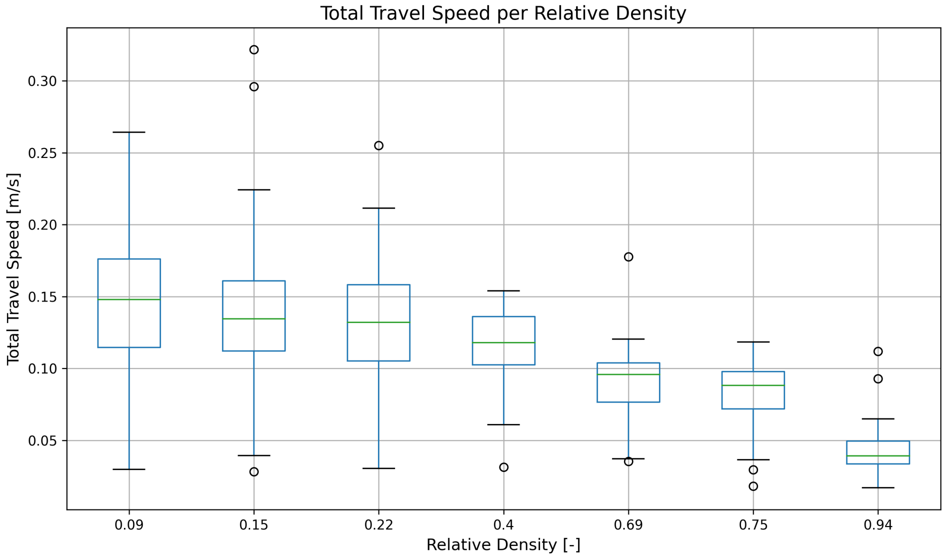

Figure E.1: Total travel speed for all density categories, based on manually measured total travel times.

tions differ. The test was performed by pooling both groups, ranking all values, and then summing the ranks for each group. These rank sums were used to calculate the U statistic, which was then compared to a critical value to assess statistical significance. This process is repeated for each pair of groups.

To take the increasing risk of false positives into account that comes with performing multiple pairwise comparisons, the Bonferroni correction was applied. This method adjusts the significance threshold by dividing the usual p-value cut-off (in this research set to be 0.05) by the number of tests conducted. While the Bonferroni correction effectively reduces the chance of incorrectly declaring a result significant (Type I error), it is conservative and can increase the likelihood of missing true effects (Type II error) (Wikipedia contributors 2025).

The results presented in Table E.1 show that, using a significance threshold of 0.05, many group pairs exhibit statistically significant differences in transport speed. Specifically, lighter particles (3g to 13g) are significantly faster than heavier particles (23g to 32g) when compared across these weight ranges. Differences between adjacent groups, especially among the lighter particles, tend to be non-significant more often, which is in agreement with the expectation that small incremental changes in weight produce only minor differences in drift speed. For instance, particles in the 3g (Relative Density = 0.09), 5g (RD = 0.15), and 7g (RD = 0.23) categories do not differ significantly from each other, yet each is significantly different from all heavier particle groups. Overall, this analysis confirms a clear trend of increasing transport time as particle weight increases, with significant differences emerging primarily between lighter and heavier particle classes.

Table E.1: Mann–Whitney U test results with Bonferroni correction

Particle Weight (PW) Group 1	PW Group 2	U statistic	Raw p-value	Bonferroni corrected p
3g	25g	1202.0	7.74e-16	1.63e-14
5g	25g	1516.0	1.37e-13	2.88e-12
3g	32g	108.5	3.16e-12	6.63e-11
3g	23g	1356.5	7.93e-12	1.66e-10
5g	32g	143.0	9.34e-12	1.96e-10
7g	32g	145.5	9.36e-12	1.97e-10
13g	32g	77.5	1.87e-11	3.93e-10
7g	25g	1792.5	2.23e-11	4.68e-10
13g	25g	1161.0	1.91e-10	4.00e-09
5g	23g	1667.5	9.10e-10	1.91e-08
23g	32g	188.0	2.95e-09	6.19e-08
25g	32g	268.5	1.80e-08	3.78e-07
7g	23g	1986.0	1.81e-07	3.80e-06
13g	23g	1286.5	3.11e-07	6.52e-06
3g	13g	2194.0	3.08e-04	6.47e-03
3g	7g	3826.5	1.91e-02	4.01e-01
5g	13g	2739.5	2.93e-02	6.16e-01
23g	25g	2497.5	3.35e-02	7.03e-01
5g	7g	4615.0	4.10e-01	1.00e+00
7g	13g	3034.5	1.84e-01	1.00e+00
3g	5g	4082.5	1.13e-01	1.00e+00

E.0.2. Zonal Travel Velocity

After assessing the total travel velocity, a further step in the processing and analysis phase consisted of dividing the flume into four main zones (shoaling, breaking, surf, Run-up) and computing the travel velocity of a sample of particles for each zone. For this purpose, some of the top-view videos were visually inspected. The goal was to detect a potential trend in travel velocity within specific zones of the flume. To achieve this, the minimum number of trajectories required to identify a significant difference between the tested conditions was analysed. As a result, the trajectories of five particles for each relative density step were manually observed.

The definition of the edges of the zones remained valid for all the relative density steps as described in 3.2.2 with the exception of the end of the swash zone. Particles with different weights stabilised on the beach at different locations; therefore, the last zone was varied between the different tested conditions.

Five particles for each tested condition were manually observed travelling the flume across the three zones. The time a particle entered and left each zone was recorded, and the travel time for each zone was computed. This was then divided by the length of the relevant zone to obtain the zonal travel velocity. This was done to better understand whether the observed variation in total travel velocity computed according to Section E.0.1 could be linked to a specific location along the length of the flume and therefore a different moment in the wave evolution. The result of this method is shown in Figure E.2, which shows that, in general, the velocities throughout the zones are higher as the particles have lower relative densities. Throughout the different categories, especially in the breaking and surf zone the variation is very visible. Based on this initial analysis, it was concluded that density has a strong and varying influence on particle drift depending on the wave zone. Therefore, further analysis should investigate how drift depends on density across different segments of the flume to better capture these zone-specific differences.

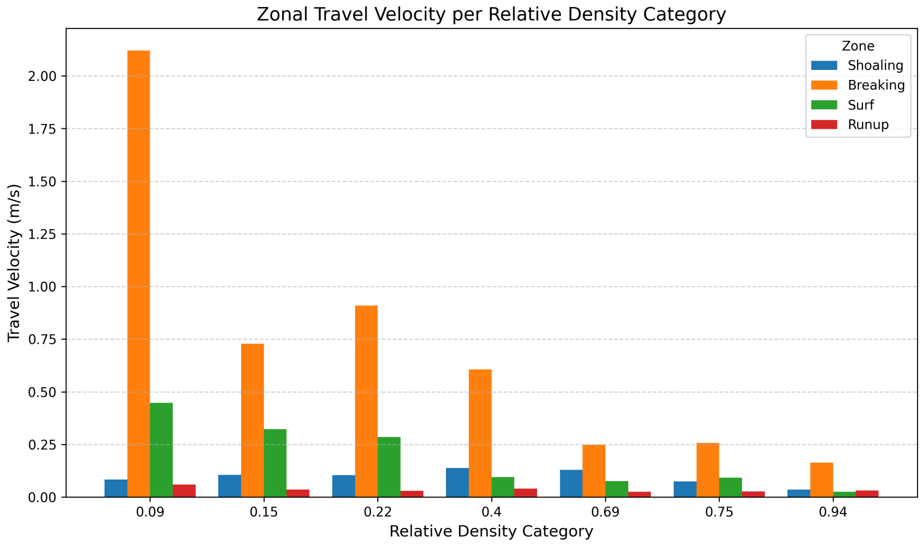

Figure E.2: Zonal travel speed for all Density Categories obtained by manually tracking approximately 5 particles per category.

Legend: ▬ 100% overlap ▬ 90% overlap with minimal adjustments ▬ 0% overlap

F

Comparison of YOLO and Tracker for Trajectory Validation

Section 3.6.4 outlines the use of Tracker, a software tool employed to validate the performance of the YOLO tracking algorithm. A subset of particles was tracked using Tracker's auto-tracking function, with manual tracking applied where needed. Unlike YOLO, Tracker was monitored throughout the process to ensure completeness as data points missed by auto tracker were manually filled in, resulting in highly reliable and continuous trajectories. However, this approach is very labour intensive and therefore unsuitable for processing the full dataset used in this research.

The high-quality Tracker trajectories were then compared to YOLO-tracked trajectories, which had been processed using the custom method developed in this study, including interpolation steps. The results of which are shown in the figures below in figures F.1 and F.2. Based on the precise overlap of trajectories in both figures, it was concluded that the Yolo algorithm, the processing method including the filters and lastly the interpolation was working very well and the data used in this research is reliable. It can be seen though that trajectories are lost using Yolo, which indicates that several trajectories were not tracked well enough to surpass the filters. Improving the Tracking algorithm could potentially yield an even higher number of trajectories from the video material used in this research.

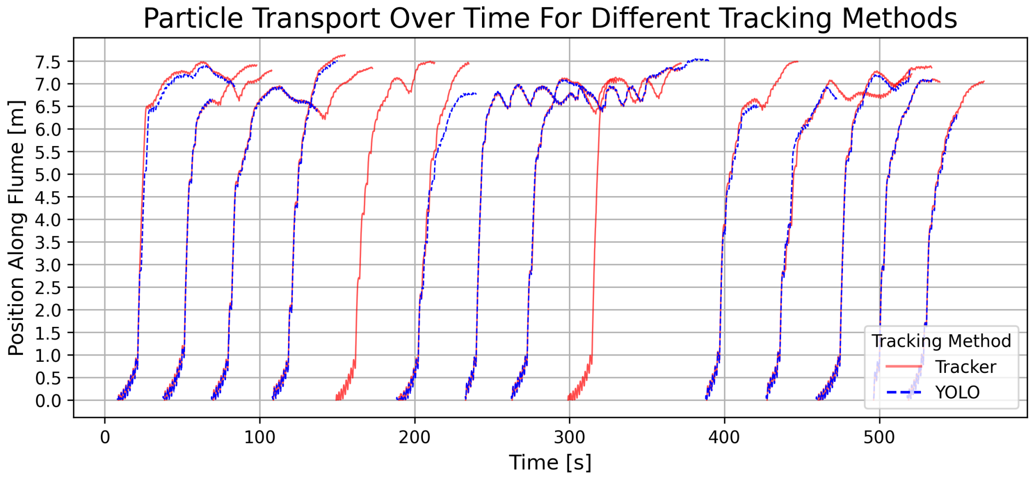

Figure F.1: Particle trajectories (distance over time) processed using different Tracker methods (Tracker and YOLO). The data consists of a mix of particles with relative densities 0.09, 0.15 and 0.23 [-] originated from experimental campaign Run 2.

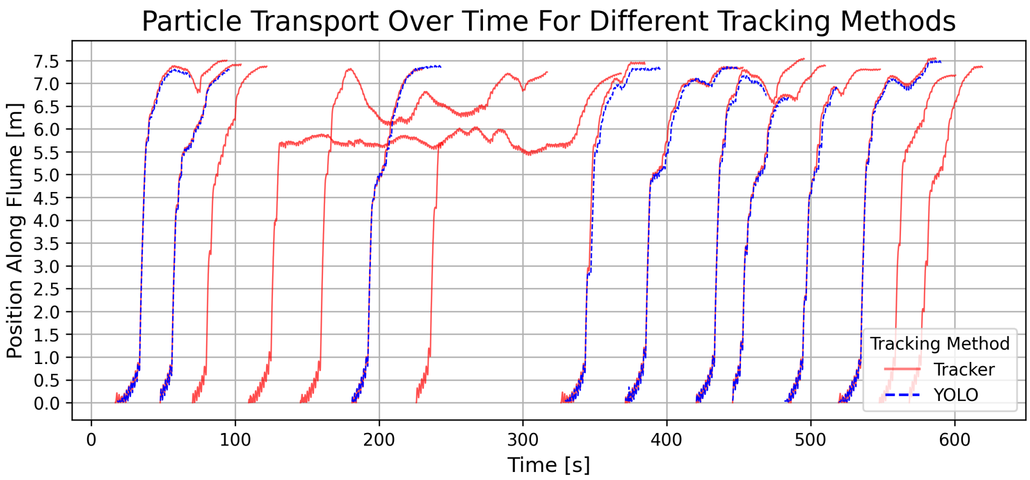

Figure F.2: Particle trajectories (distance over time) processed using different Tracker methods (Tracker and YOLO). The data consists of a mix of particles with relative densities 0.09, 0.15 and 0.23 [-] originated from experimental campaign Run 3.

Legend: ▬ 100% overlap ▬ 90% overlap with minimal adjustments ▬ 0% overlap

G

YOLO Algorithm Performance

The performance of the trained YOLO model, used to detect green, pink, and yellow particles in the experimental footage, is illustrated in the normalized confusion matrix shown in Figure G.1. The three different colours were used to distinguish between particles of different density categories. This matrix offers a overview of the accuracy for each colour category.

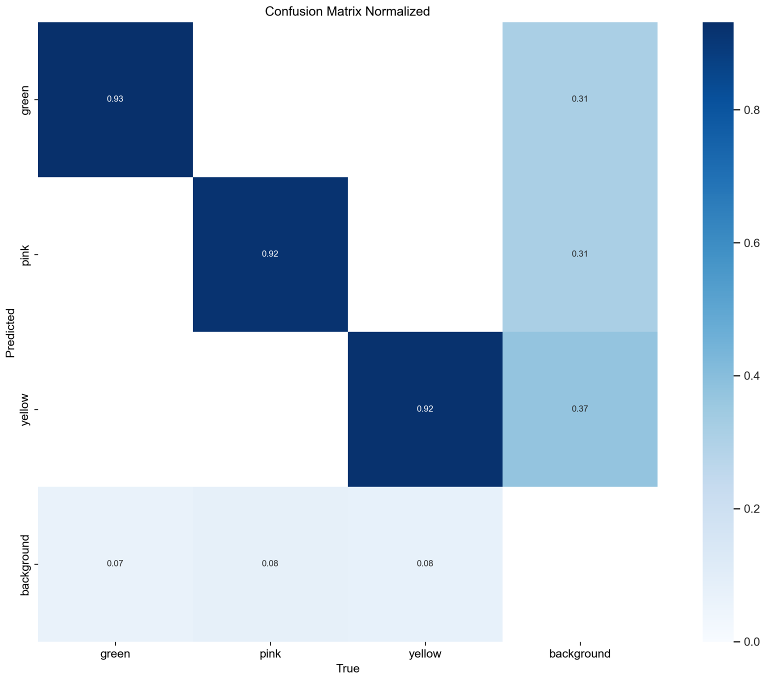

Figure G.1: Normalized confusion matrix showing the classification performance of the YOLO model for each particle class and the background.

As seen in the figure, the model achieves high classification accuracy for all three particle classes being 93% for green particles and 92 % for pink and yellow, showing that the model is highly effective in identifying the particles of interest.

However, a notable issue is the misclassification of background pixels as particles, especially:

- 31% of background pixels are misclassified as green or pink

- A significant 37% of background pixels are misclassified as yellow

This tendency suggests over-detection, particularly for the yellow class. This can be attributed to the use of yellow tape (a yellow very similar to the particle yellow) placed along the flume floor, leading to false positives.

Despite this, the core detection performance for the actual particle classes remains strong, validating the model's applicability for trajectory extraction in this research. Still, caution should be exercised when interpreting results involving the yellow class in regions with visual background contamination.

H

Code and Data Availability

The main Python scripts used in the context of this research are made available at the following GitHub repository:

`https://github.com/camicocozza/Cocozza_Swuste_MSc_Plastic_Beaching.git`

It includes:

- ”Camera calibration” folder: contains a Jupyter notebook used to perform camera calibration and assess the level of image distortion.
- ”YOLO_Tracking” folder: contains the necessary scripts to perform particle tracking as described in Section 3.6.3. Additionally, the trained model is attached to allow for reproducibility of the current methodology.
- ”SWASH” folder: contains the input files necessary to run the SWASH simulations.

These Python scripts were developed collaboratively by Camilla Cocozza and Leanne Swuste.

Legend: ▬ 100% overlap ▬ 90% overlap with minimal adjustments ▬ 0% overlap

---

I

Contribution acknowledgment

This research serves as the foundation for an individual MSc thesis and is therefore presented as a singular document. However, the methodology applied in this study was developed jointly by Camilla Cocozza and Leanne Swuste, and large parts of the Theoretical Background and Methodology chapters within this document were written in collaboration. To acknowledge these shared contributions, this appendix provides a detailed overview of the individual inputs to ensure transparency and clarity for the reader.

A colour-coding system is used throughout this document to indicate individual contributions. A coloured line on the left side of the text identifies which author(s) were responsible for each section.

1. Complete overlap: These sections were written in collaboration between both authors and overlaps exactly between the two MSc thesis reports. The individual contribution of both students within these exactly overlapping texts can be found below in table I.1
2. Partial Overlap: These sections were originally written in collaboration by both authors but were later adapted slightly to align with the specific research questions addressed in each thesis. While the core content remains largely the same (with approximately 85–95% overlap), minor modifications and additions were made to tailor the text to each research topic. A breakdown of individual contributions within these sections is provided in the table I.1.
3. Individual: These sections are written individually for each report by the respective author. These sections are specific to the topic addressed in this report.

Legend: ▬ 100% overlap ▬ 90% overlap with minimal adjustments ▬ 0% overlap

---

Table I.1: Overview of Chapter Contributions and Feedback

Section	Written by	Feedback from
Marine Plastic Debris	Contributions of both	x
Wave Basics	Contributions of both	x
Coastal Wave Dynamics	Contributions of both	x
Wave Propagation Velocities	Contributions of both	x
Experimental Facility	Camilla	Leanne
Wave Gauges	Camilla	Leanne
Electromagnetic Flow Meter	Camilla	Leanne
Camera Setup	Leanne	Camilla
Spin-up Time	Leanne	Camilla
Instrument Deployment Strategy	Leanne	Camilla
Tipping Point	Leanne	Camilla
Experimental Procedure	Camilla	Leanne
Hydrodynamic Conditions	Leanne	Camilla
Swash Model	Camilla	Leanne
Particle detection YOLO	Leanne	Camilla
Tracking Algorithm	Camilla	Leanne
Trajectory Validation	Camilla	Leanne
Trajectory Processing	Camilla	Leanne
Phase Speed	Leanne	Camilla
Crest Speed	Leanne	Camilla
Stokes Drift	Camilla	Leanne
Total Travel Velocity	Leanne	Camilla
Zonal Travel Velocity	Camilla	Leanne
Swash Model	Camilla	Leanne